Mon. Not. R. Astron. Soc. **000**, 000–000 (0000) Printed 3 March 2014 (MN LATEX style file v2.2)

Possible Indirect Confirmation of the Existence of Pop III Massive Stars by Gravitational Wave

Tomoya Kinugawa[1] ⋆, Kohei Inayoshi[1], Kenta Hotokezaka [1], Daisuke Nakauchi,[1] Takashi Nakamura[1]

[1] *Department of Physics, Graduate School of Science, Kyoto University, Kyoto 606-8502, Japan*

arXiv:1402.6672v2 [astro-ph.HE] 28 Feb 2014

3 March 2014

ABSTRACT

We perform population synthesis Monte Carlo simulations for the formation rate and the mass spectrum of Population III (Pop III) coalescing binary neutron stars (NS-NSs), neutron star – black hole binaries (NS-BHs), and binary black holes (BH-BHs) which merge within the age of the universe. We upgrade the open numerical code (Hurley, Tout & Pols 2002) for Population I (Pop I) stars to Pop III stars. We found that the typical mass of Pop III black holes is ~ 30 $M_\odot$ so that the inspiral chirp signal of gravitational waves can be detected up to ~ 1500 Mpc ($z = 0.28$) by KAGRA, Adv. LIGO, Adv. Virgo and GEO network. Our new simulations suggest that the expected detection rate of the coalescing Pop III BH-BHs is $140\ (68) \cdot (\mathrm{SFR_p}/10^{-2.5}\ M_\odot\ \mathrm{yr}^{-1}\ \mathrm{Mpc}^{-3}) \cdot \mathrm{Err_{sys}}$ events yr^{-1} for the flat (Salpeter) initial mass function (IMF), respectively, where $\mathrm{SFR_p}$ and $\mathrm{Err_{sys}}$ are the peak value of the Pop III star formation rate and the possible systematic errors due to the assumptions in Pop III Monte Carlo population synthesis, respectively. The case of $\mathrm{Err_{sys}} = 1$ corresponds to the reference case where the parameters of the binary evolution and initial conditions for the Pop I case are adopted. In general, $\mathrm{Err_{sys}}$ could deviate from the unity. For Einstein Telescope like third generation detectors, the detection rate is ~ 80 times more and the detection range is up to $z \sim 3$. From the observation of the chirp signal of the coalescing Pop III BH-BHs, we can determine both the mass and the redshift of the binary for the cosmological parameters determined by Planck satellite. Our simulations suggest that the cumulative redshift distribution of the coalescing Pop III BH-BHs depends almost only on the cosmological parameters. We might be able to confirm the existence of PopIII massive stars of mass ~ 30 $M_\odot$ by the detections of gravitational waves if the merger rate of the Pop III massive BH-BHs dominates that of Pop I BH-BHs. Note that expected fiducial rate of $2.5\ (1.2) \times 10^{-8}$ events yr^{-1} Mpc^{-3} for the flat (Salpeter) IMF, respectively, is consistent with the upper limit of $\sim 10^{-7}$ events yr^{-1} Mpc^{-3} by LIGO-Virgo (S6/VSR2/VSR3) (Aasi et al. 2013).

1 INTRODUCTION

Gravitational-wave astronomy with KAGRA[1], Adv. LIGO[2], Adv. Virgo[3], and GEO[4] will reveal the formation and evolution of binaries through the observed merger rates of compact binaries, such as binary neutron stars (NS-NSs), neutron star – black hole binaries (NS-BHs), and binary black holes (BH-BHs). For this gravitational wave astronomy, estimates of the merger rate of compact binaries play key roles to develop observational strategy and to translate the observed merger rates into the binary formation and evolution processes.

There are two methods to estimate the merger rate of compact binaries. One is to use observational facts such as the observed NS-NSs whose coalescence time due to the emission of gravitational waves is less than the age of the universe. Taking into account the observation time, the sensitivity of the radio telescope, the luminosity function of pulsars and the beaming factor so on, the probability distribution function of the merger rate can be found. For example, Kalogera, Kim, Lorimer et al. (2004b) found that the

[1] http://gwcenter.icrr.u-tokyo.ac.jp/en/
[2] http://www.ligo.caltech.edu/
[3] http://www.ego-gw.it/index.aspx/
[4] http://www.geo600.org/

© 0000 RAS

event rate of the coalescing NS-NSs is in the range from 10^{-5} events yr^{-1} galaxy^{-1} to 4×10^{-4} events yr^{-1} galaxy^{-1} at the 99 % confidence level (see their Fig. 2)[5].

The merger rate of NS-NSs can be restricted by the rate of the observed Type Ib and Ic supernovae, supposing that the formation of NS-NSs really starts from the massive binary zero age main sequence (ZAMS) stars. This is because the formation of the second neutron star should occur in association with Type Ib and Ic supernovae in which the H-rich envelope and the He-layer are lost, respectively, otherwise the binary disrupts due to the sudden large mass loss at the supernova explosion[6]. Under the assumption of the equality of the formation rate to the merger rate, the merger rate of the NS-NSs is limited by the Type Ib and Ic supernova rate of $\sim 10^{-3}$ events yr^{-1} galaxy^{-1} (Cappellaro et al. 1997, 1999; Li et al. 2011). Therefore the maximum rate of 4×10^{-4} events yr^{-1} galaxy^{-1} by Kalogera, Kim, Lorimer et al. (2004b) implies that $\sim$ 40 % of the Type Ib and Ic supernovae is associated with the formation of NS-NSs with the coalescence time less than the age of the universe. This percentage seems to be too large. We also note here that under the assumption that central engine of short gamma ray bursts are coalescing binary neutron stars, one can use the observations of short gamma ray bursts to estimate the coalescing rate (Coward et al. (2012) and references cited there).

The dynamical interaction in a globular cluster is another route to the formation of NS-NSs since there exists PSR2127+11C, which is contained in a NS-NS system, in the globular cluster M15 (Prince, Anderson, Kulkarni & Wolszczan 1991). The age of the globular cluster is $\sim 10^{10}$ yr so that all the massive stars ended their life and the young pulsars do not exist. The coalescence time of PSR2127+11C is $\sim 2\times10^{8}$ yr which is much smaller than the age of the globular cluster so that it was formed by three body interactions such as the collision of neutron star – white dwarf binary or neutron star – dwarf star binary with a single neutron star. Since there exists only one NS-NS observed in the globular cluster, it is difficult to estimate the merger rate. Theoretical simulation is the only method at present (Grindlay, Portegies Zwart & McMillan 2006; Ivanova, Heinke, Rasio et al. 2008).

The another method to estimate the merger rate of compact binaries is to use theoretical computation based on the hypothetical assumptions of binary formation and evolution. For NS-BHs and BH-BHs, in particular, there exists no observations so that we can only use theoretical estimates. The merger rates of compact binaries of Population I (Pop I) stars were estimated by many authors (Belczynski, Kalogera & Bulik 2002; Belczynski et al. 2007; Belczynski & Dominik 2012). Dominik et al. (2012) computed the merger rates for the progenitor stars of metallicity $Z = 0.1\ Z_\odot$ and found that the number of the coalescing BH-BHs increases compared with that for $Z = Z_\odot$. Dominik et al. (2013) adopted a certain model of the star formation rate and the chemical evolution of the metallicity Z to compute the cumulative redshift distribution of the coalescing compact binaries.

In this paper, we focus on the compact binary merger originated from Population III stars (Pop III stars) as gravitational wave sources. Pop III stars are the first stars after the Big Bang which are formed from metal-free gas (Omukai & Nishi 1998; Bromm, Coppi & Larson 2002; Abel, Bryan & Norman 2002; Yoshida, Omukai & Hernquist 2008; Greif et al. 2012). The simulations of a rotating primordial gas cloud suggest that the formation of Pop III star binaries and multiple star systems are frequent (Machida et al. 2008; Stacy et al. 2010). The main differences of our work from Dominik et al. (2012, 2013) are the following two: (1) we focus on metal-free Pop III stars and (2) consider the star formation history including the transition to metal-enriched stars (see §4). The observed merger rate will be the sum of our work and Dominik et al. (2013).

There are at least three differences between Pop III and Pop I compact binaries. First of all, Pop III stars are more massive than Pop I stars (McKee & Tan 2008; Hosokawa et al. 2011, 2012; Stacy et al. 2012) with mass $10-100$ M$_\odot$ so that Pop III star binaries probably evolve into BH-BHs. Secondly, since the typical formation time of Pop III stars is at $z\sim10$, even if the coalescence time is comparable to the age of the universe, they merge at present and contribute to the sources of gravitational waves for KAGRA, Adv. LIGO, Adv. Virgo, and GEO network. Therefore, if Pop III NS-NSs were formed, they might merge at present so that their rate is free from the constraint of the observed NS-NSs as well as Type Ib and Ic supernova rate discussed in the previous paragraphs. Thirdly, Pop III black holes are expected to be more massive than Pop I black holes due to less mass loss so that the resulting gravitational waves are easier to detect, since the detectable distance is proportional to 5/6 power of the chirp mass ($M_{\rm chirp}$) of a binary defined by $M_{\rm chirp}=(M_1M_2)^{3/5}/(M_1+M_2)^{1/5}$ (Seto, Kawamura & Nakamura 2001), where M_1 and M_2 are the mass of each compact object.

The idea of Pop III compact binaries as gravitational-wave sources has been considered by Belczynski, Bulik & Rudak (2004) and Kowalska, Bulik & Belczynski (2012). However they considered very massive Pop III stars with mass over hundred solar masses. Recent study shows that the typical mass of Pop III stars is set to 10–100M$_\odot$ by the stellar radiation feedback on the accretion flow (Hosokawa et al. 2011, 2012). Therefore, in this paper, we calculate 10^6 Pop III binary evolutions with the mass range of 10–100M$_\odot$ to estimate merger rates and mass distribution of Pop III compact binaries. In order to calculate Pop III binary evolutions, we upgrade Hurley's binary population synthesis code (Hurley, Tout & Pols 2002) for the Pop I star to Pop III star case.

This paper is organized as follows. We describe Pop III single star evolution in §2.1, the method to calculate Pop III

[5] Note here that there are errors in Kalogera, Kim, Lorimer et al. (2004a) so that the rates in Kalogera, Kim, Lorimer et al. (2004b) are the correct ones.

[6] If more than half of the total mass is suddenly lost at the supernova explosion, the binary disrupts.

binary star evolutions in §2.2, numerical calculation methods in §2.3. In §3, we present the results of simulations and argue properties of Pop III compact binaries. We compare Pop III compact binary mergers with Pop I compact binary mergers in §3.2. In §4, we describe the Pop III compact binary merger rates. §5 is devoted to the discussions. In Appendix, we show the details of our numerical methods, the comparison of our results with Hurley's ones and the convergence check of our simulations. We adopt the cosmological parameters of $(\Omega_\Lambda, \Omega_{\rm m}) = (0.6825, 0.3175)$ and the Hubble parameter of $H_0 = 67.11$ km s^{-1} Mpc^{-1} (Planck Collaboration 2013). Those who are not interested in the details of the methods in numerical simulations can skip §2.

2 METHOD OF BINARY POPULATION SYNTHESIS SIMULATIONS

2.1 Single star evolution

2.1.1 Population III stars

Pop III stars are formed in the early universe from primordial gas, i.e., without heavy elements. The star formation process of Pop III stars has been investigated by many authors (Tegmark et al. 1997; Omukai & Nishi 1998; Bromm, Coppi & Larson 2002; Yoshida, Omukai & Hernquist 2008; Greif et al. 2012). According to their studies, the differences of the chemical compositions lead to the following three features of Pop III stars compared with Pop I stars:(1) more massive > 10 M$_\odot$ (2) smaller stellar radius for the same mass (3) less mass loss by stellar wind. Since these features play key roles in a single stellar evolution and binary interactions (see also Sec. 2.2), we briefly summarize these features of Pop III stars in what follows.

In primordial gas, the H_2-line emission is the main cooling process, which is less efficient than the dust cooling as in Pop I star formation. Since the gas temperature is kept hotter, typically massive cloud collapses and forms protostars at the center. Recent numerical simulations (e.g., Hosokawa et al. 2011, 2012; Stacy et al. 2012) suggest that the Pop III protostar can grow to $\sim$ several 10 M$_\odot$ until the radiation feedback halts the gas accretion onto the central protostar. Therefore, Pop III stars at the ZAMS stage are typically more massive than Pop I stars of mass ~ 1 M$_\odot$.

When the protostar reaches the Zero Age Main Sequence (ZAMS) stage, the star contracts until the central temperature rises above 10^8 K to generate C via triple-alpha reaction so that CNO-cycle starts (Marigo et al. 2001). Thus, stable structure of Pop III ZAMS star has the smaller radius than that of Pop I stars. As a result, the binary interaction for Pop III stars becomes more weak than those for Pop I stars. Figure 1 shows the Hertzsprung-Russell (HR) diagram for Pop III stars over the mass range of $10 \leqslant M \leqslant 100$ M$_\odot$ from the ZAMS stage to the beginning of the C-burning stage. In Pop III star case, the central temperature is so high that the He-burning soon begins after the end of the H-burning. Therefore, the resultant stellar evolution at the post main sequence stage is different from the usual Pop I star case (Kippenhahn & Weigert 1990).

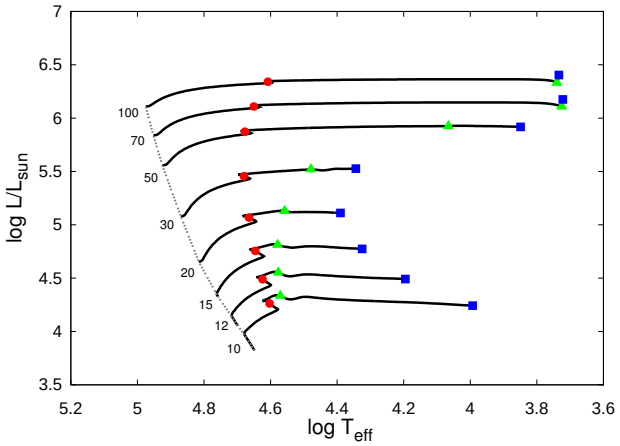

Figure 1. The Hertzsprung-Russell (HR) diagram for the Pop III stars of mass 10 M$_\odot$ $\leqslant M \leqslant$ 100 M$_\odot$ using the data taken from Marigo et al. (2001). The number attached to each solid curve is the mass of each star in unit of M$_\odot$. The dashed line shows the ZAMS (Zero Age Main Sequence) stars. Red circles, green triangles and blue squares correspond to the beginning of He-burning, the end of the He-burning and the beginning of the C-burning, respectively.

The mass loss due to the stellar wind and pulsation has impacts on the stellar evolution and the mass of the remnant compact objects. For Pop III star case, such mass-loss processes do not operate because of no heavy elements at the stellar surface (e.g. Baraffe, Heger & Woosley 2001; Inayoshi, Hosokawa & Omukai 2013). Therefore, we neglect the effect of the mass loss on the stellar evolution.

2.1.2 Fitting formulae of Pop III steller evolution

In order to include the single PopIII star evolution to the binary population synthesis simulation code given by Hurley, Tout & Pols (2002), we need to construct the fitting formula to the stellar radius and the core mass as a function of time since it consumes too long cpu time to numerically evolve Pop III stars up to the C-burning phase in each population synthesis. Using the results of stellar evolution for Pop III stars calculated by Marigo et al. (2001), we here present fitting formulae of the stellar radius and core mass as functions of the stellar mass M and the time (t) from the birth of a star.

We basically fit the stellar radii of Pop III stars in the same way as Hurley, Pols & Tout (2000) did for Pop I stars. As shown in Fig. 1, we divide the life of Pop III stars into the four characteristic phases: (1) H-burning phase (from the ZAMS to red circle), (2) the He-burning phase (from red circle to green triangle), (3) the He-shell burning phase (blue square), and (4) after the C-ignition. In the followings, we show the fitting formulae in each phase. We use the subscripts H, He, HeS and C to each physical variables such as the radius and the mass to show the H-burning phase, the He-burning phase, the He-shell burning phase and the C-burning phase, respectively. The superscripts b and e de-

note the beginning and the end of each phase, respectively. Basically, the fitting formulae are expressed as the forms of polynomials of the mass and age. In other cases, we will mention how to obtain each formulae.

(1) H-burning phase

In order to characterize the stellar radius of the H-burning phase, we first need to obtain the stellar radius of the ZAMS ($R_{\rm ZAMS}$), the stellar radius at the end of the main sequence, and the H-burning time $t_{\rm H}$, which can be expressed as

$$\begin{aligned}(R_{\rm ZAMS}/{\rm R}_\odot) &= 1.22095 + 2.70041\times10^{-2}(M/10\ {\rm M}_\odot)\\ &+ 0.135427(M/10\ {\rm M}_\odot)^2 - 1.95541\times10^{-2}(M/10\ {\rm M}_\odot)^3\\ &+ 8.7585\times10^{-4}(M/10\ {\rm M}_\odot)^4, \end{aligned} \quad (1)$$

$$\begin{aligned}(R^{\rm e}_{\rm H}/{\rm R}_\odot) &= 0.581309 + 2.27745(M/10\ {\rm M}_\odot)\\ &+ 6.63321\times10^{-3}(M/10\ {\rm M}_\odot)^3, \end{aligned} \quad (2)$$

and

$$\begin{aligned}(t_{\rm H}/{\rm Myr}) &= 1.78652 + 10.4323(M/10\ {\rm M}_\odot)^{-1}\\ &+ 3.70946(M/10\ {\rm M}_\odot)^{-2} + 2.04264(M/10\ {\rm M}_\odot)^{-3}, \end{aligned} \quad (3)$$

respectively.

For simplicity, we introduce the time $\tau_{\rm H}$ by $\tau_{\rm H} = t/t_{\rm H}$ and express the stellar radius $R_{\rm H}$ during H-burning phase as a function of time as

$$\begin{aligned}\log(R_{\rm H}/{\rm R}_\odot) &= \log(R_{\rm ZAMS}/{\rm R}_\odot) + a_{\rm H}\tau_{\rm H} + b_{\rm H}\tau_{\rm H}^{10}\\ &+ c_{\rm H}\tau_{\rm H}^{500} + d_{\rm H}\tau_{\rm H}^{3}, \end{aligned} \quad (4)$$

where

$$a_{\rm H} = \begin{cases} -0.430873 + 0.520408(M/10\ {\rm M}_\odot)\\ -7.99762\times10^{-2}(M/10\ {\rm M}_\odot)^2\\ -3.55095\times10^{-3}(M/10\ {\rm M}_\odot)^3\\ \qquad (10\ {\rm M}_\odot \leqslant M < 30\ {\rm M}_\odot),\\ 0.476498 - 9.07537\times10^{-2}(M/10\ {\rm M}_\odot)\\ +1.43538\times10^{-2}(M/10\ {\rm M}_\odot)^2\\ -6.89108\times10^{-4}(M/10\ {\rm M}_\odot)^3\\ \qquad (30\ {\rm M}_\odot \leqslant M \leqslant 100\ {\rm M}_\odot), \end{cases} \quad (5)$$

$$b_{\rm H} = \begin{cases} 0.669345 - 1.5518(M/10\ {\rm M}_\odot) + 1.15116(M/10\ {\rm M}_\odot)^2\\ -0.254811(M/10\ {\rm M}_\odot)^3\\ \qquad (10\ {\rm M}_\odot \leqslant M < 20\ {\rm M}_\odot),\\ 3.02801\times10^{-2} + 6.48197\times10^{-2}(M/10\ {\rm M}_\odot)\\ -6.64582\times10^{-3}(M/10\ {\rm M}_\odot)^2\\ +3.37205\times10^{-4}(M/10\ {\rm M}_\odot)^3\\ \qquad (20\ {\rm M}_\odot \leqslant M \leqslant 100\ {\rm M}_\odot), \end{cases} \quad (6)$$

$$c_{\rm H} = \begin{cases} 5.63328\times10^{-2} - 9.88927\times10^{-2}(M/10\ {\rm M}_\odot)\\ +2.00071\times10^{-2}(M/10\ {\rm M}_\odot)^2\\ \qquad (10\ {\rm M}_\odot \leqslant M < 30\ {\rm M}_\odot),\\ -0.128025 + 3.63928\times10^{-2}(M/10\ {\rm M}_\odot)\\ -5.43719\times10^{-3}(M/10\ {\rm M}_\odot)^2\\ +2.75137\times10^{-4}(M/10\ {\rm M}_\odot)^3\\ \qquad (30\ {\rm M}_\odot \leqslant M \leqslant 100\ {\rm M}_\odot), \end{cases} \quad (7)$$

and

$$d_{\rm H} = \log(R^{\rm e}_{\rm H}/R_{\rm ZAMS}) - a_{\rm H} - b_{\rm H} - c_{\rm H}. \quad (8)$$

In Fig. 2, we compare the fitting formula with the numerical data as a function of time. The vertical and horizontal axes are $\log(R_{\rm H}/R_{\rm ZAMS})$ and $\tau_{\rm H} \equiv t/t_{\rm H}$, respectively. The red line and the crosses denote the fitting formula of stellar radius Eq. (4) and the computed data given by Marigo et al. (2001), respectively. The green, blue, pink and light blue lines represent the contributions from the second, third, fourth and fifth term of the fitting formula (Eq. (4)), respectively. Each panel refers to the stellar mass (a) 10 $\rm M_\odot$, (b) 30 $\rm M_\odot$, (c) 50 $\rm M_\odot$ and (d) 100 $\rm M_\odot$, respectively. For low mass cases, stellar radii can be expressed mainly by the fifth term of $d_{\rm H}\tau_{\rm H}^3$ (light blue line), whereas for high mass cases they are mainly approximated by the terms of $a_{\rm H}\tau_{\rm H}$ (green line) and $b_{\rm H}\tau_{\rm H}^{10}$ ($\tau_{\rm H} \gtrsim 0.5$, blue line). Just before the end of the main sequence ($\tau_{\rm H} \gtrsim 0.99$), the stellar radius dramatically shrinks, because H has been exhausted in the central core. This prominent feature is called as the *main sequence hook* (see also Fig. 1) and is well described by the term of $c_{\rm H}\tau_{\rm H}^{500}$ (pink line) in Eq. (4). The inset in each figure is the magnification of the contribution from each term for $0.99 < \tau_{\rm H} < 1$ to show the effect of this term.

Fig. 3 shows the time averaged root mean square (rms) errors of our fitting formula as a function of the stellar mass. The red line is rms during the H-burning phase (Eq. 4), which shows that our fitting formula has the relative accuracy within 2 % of the models of Marigo et al. (2001).

(2) He-burning phase

At the end of the main sequence phase, the He-burning smoothly begins in the central core for massive Pop III stars ($\gtrsim 10\ {\rm M}_\odot$) without the Hertzsprung gap, because the central temperature during the H-burning phase is already high enough to ignite He ($\gtrsim 10^8$ K). Therefore, in this paper, the beginning of the He-burning phase is assumed to be the same time as the end of the H-burning phase ,i.e., $R^{\rm b}_{\rm He} = R^{\rm e}_{\rm H}$.

The stellar radii at the end of the He-burning phase $R^{\rm e}_{\rm He}$ and the lifetime of the He-burning phase ($t_{\rm He}$) is approxi-

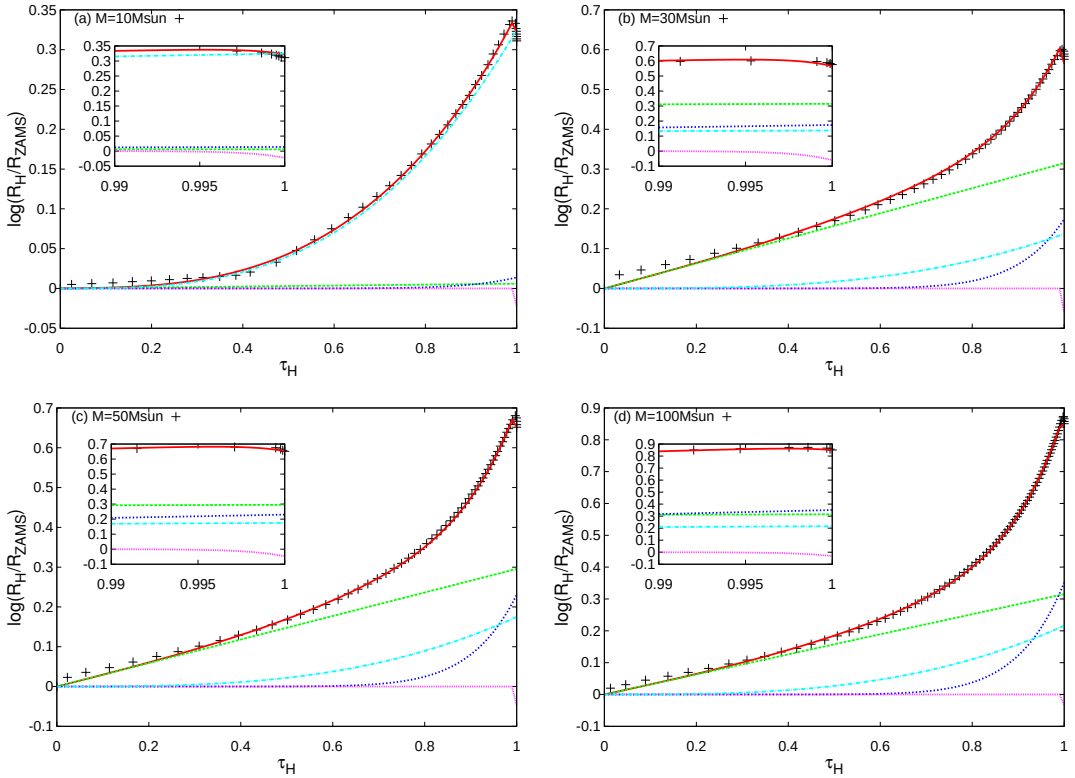

Figure 2. The comparison of the fitting formula with the numerical data as a function of time. The vertical and horizontal axises are $\log(R_{\rm H}/R_{\rm ZAMS})$ and $\tau_{\rm H} \equiv t/t_{\rm H}$ with $t_{\rm H}$ being the H-burning time, respectively. The red line is the fitting formula of stellar radius (Eq. 4) and the crosses are computed data given by Marigo et al. (2001). The green, blue, pink and light blue lines, represent the contributions from the second, third, fourth and fifth term of the fitting formula (Eq. 4), respectively. Each panel refers to the stellar mass (a) 10 $M_\odot$, (b) 30 $M_\odot$, (c) 50 $M_\odot$ and (d) 100 $M_\odot$, respectively. For the low mass case, the stellar radius can be expressed mainly by the fifth term of $d_{\rm H}\tau_{\rm H}^3$ (light blue line), whereas for high mass case they are mainly expressed by the terms of $a_{\rm H}\tau_{\rm H}$ (green line) and $b_{\rm H}\tau_{\rm H}^{10}$ ($\tau_{\rm H} \gtrsim 0.5$, blue line). Around the end of the main sequence lifetime ($\tau_{\rm H} \gtrsim 0.99$), the stellar radii dramatically shrink, because H has been exhausted in the central core. This prominent feature is called as the *main sequence hook* (see also Figure 1) and is well described by the term of $c_{\rm H}\tau_{\rm H}^{500}$ (pink line) in Eq. (4). The inset in each figure is the magnification of the contribution from each term for $0.99 \leqslant \tau_{\rm H} \leqslant 1$ to show the effect of this term.

mated by

$$\log(R^{\rm e}_{\rm He}/{\rm R}_\odot) = \begin{cases} -7.23005 \times 10^{-2} + 0.814329(M/10\ {\rm M}_\odot) \\ -0.252995(M/10\ {\rm M}_\odot)^2 \\ +5.88465 \times 10^{-2}(M/10\ {\rm M}_\odot)^3 \\ -4.28501 \times 10^{-3}(M/10\ {\rm M}_\odot)^4 \\ \qquad (10\ {\rm M}_\odot \leqslant M < 50\ {\rm M}_\odot), \\ -2.40224 + 1.32865 \times (M/10\ {\rm M}_\odot) \\ -7.65293 \times 10^(-2)(M/10\ {\rm M}_\odot)^2 \\ \qquad (50\ {\rm M}_\odot \leqslant M \leqslant 100\ {\rm M}_\odot), \end{cases} \tag{9}$$

and

$$\log(t_{\rm He}/{\rm Myr}) = \begin{cases} 6.95516 - 1.17529(M/10\ {\rm M}_\odot) \\ +0.264783(M/10\ {\rm M}_\odot)^2 \\ \qquad (10\ {\rm M}_\odot \leqslant M < 20\ {\rm M}_\odot), \\ 6.13 - 0.331059(M/10\ {\rm M}_\odot) \\ +5.16053 \times 10^{-2}(M/10\ {\rm M}_\odot)^2 \\ -2.8 \times 10^{-3}(M/10\ {\rm M}_\odot)^3 \\ \qquad (20\ {\rm M}_\odot \leqslant M \leqslant 100\ {\rm M}_\odot), \end{cases} \tag{10}$$

where the normalized time $\tau_{\rm He}$ in He-burning phase is defined by

$$\tau_{\rm He} \equiv \frac{t - t_{\rm H}}{t_{\rm He}}. \tag{11}$$

Using $\tau_{\rm He}$, the fitting formula of the stellar radius during the He-burning phase is given by

$$\log(R_{\rm He}/{\rm R}_\odot) = \log(R^{\rm e}_{\rm H}/{\rm R}_\odot) + a_{\rm He}\tau_{\rm He} + b_{\rm He}\tau_{\rm He}^2 + c_{\rm He}\tau_{\rm He}^3 + d_{\rm He}\tau_{\rm He}^4 + \left(\log(R^{\rm e}_{\rm He}/R^{\rm e}_{\rm H}) - a_{\rm He} - b_{\rm He} - c_{\rm He} - d_{\rm He}\right)\tau_{\rm He}^5, \tag{12}$$

where

$$a_{\rm He} = \begin{cases} -0.891114 + 0.992291(M/10\ {\rm M}_\odot) \\ -0.500532(M/10\ {\rm M}_\odot)^2 + 7.46275 \times 10^{-2}(M/10\ {\rm M}_\odot)^3 \\ \qquad (10\ {\rm M}_\odot \leqslant M < 20\ {\rm M}_\odot), \\ 3.08883 - 3.85847(M/10\ {\rm M}_\odot) + 1.40618(M/10\ {\rm M}_\odot)^2 \\ -0.178175(M/10\ {\rm M}_\odot)^3 + 7.32187 \times 10^{-3}(M/10\ {\rm M}_\odot)^4 \\ \qquad (20\ {\rm M}_\odot \leqslant M \leqslant 100\ {\rm M}_\odot), \end{cases} \tag{13}$$

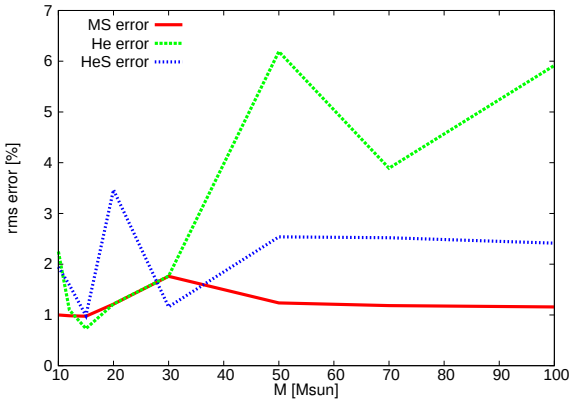

Figure 3. The time averaged root mean square (rms) errors of our fitting formulae relative to the numerical results given in Marigo et al. (2001), as a function of stellar mass. The red, green and blue lines correspond to those fitting formulae during the H-burning phase (Eq. 4), He-burning phase (Eq. 12) and He-shell burning phase (Eq. 25), respectively. We can see that our fitting formulae have relative accuracy within 2 %, 6 % and 3.5 % of numerical calculations by Marigo et al. (2001) for the H-burning, He-burning and He-shell burning phase, respectively.

$$b_{\rm He}=\begin{cases}-0.433454+0.768418(M/10\ {\rm M}_\odot)\\ \qquad(10\ {\rm M}_\odot\leqslant M<15\ {\rm M}_\odot),\\ -2.10737+1.88553(M/10\ {\rm M}_\odot)\\ \qquad(15\ {\rm M}_\odot\leqslant M<20\ {\rm M}_\odot),\\ -28.3697+33.7648(M/10\ {\rm M}_\odot)-12.2469(M/10\ {\rm M}_\odot)^2\\ +1.56514(M/10\ {\rm M}_\odot)^3-6.4361\times10^{-2}(M/10\ {\rm M}_\odot)^4\\ \qquad(20\ {\rm M}_\odot\leqslant M\leqslant100\ {\rm M}_\odot),\end{cases}\tag{14}$$

$$c_{\rm He}=\begin{cases}45.8092-114.873(M/10\ {\rm M}_\odot)+110.156(M/10\ {\rm M}_\odot)^2\\ -46.1519(M/10\ {\rm M}_\odot)^3+6.88478(M/10\ {\rm M}_\odot)^4\\ \qquad(10\ {\rm M}_\odot\leqslant M<20\ {\rm M}_\odot),\\ 85.996-100.37(M/10\ {\rm M}_\odot)+36.7017(M/10\ {\rm M}_\odot)^2\\ -4.68789(M/10\ {\rm M}_\odot)^3+0.191704(M/10\ {\rm M}_\odot)^4\\ \qquad(20\ {\rm M}_\odot\leqslant M\leqslant100\ {\rm M}_\odot),\end{cases}\tag{15}$$

and

$$d_{\rm He}=\begin{cases}-51.6917+125.87(M/10\ {\rm M}_\odot)-121.373(M/10\ {\rm M}_\odot)^2\\ +51.3681(M/10\ {\rm M}_\odot)^3-7.74452(M/10\ {\rm M}_\odot)^4\\ \qquad(10\ {\rm M}_\odot\leqslant M<20\ {\rm M}_\odot),\\ -103.871+120.228(M/10\ {\rm M}_\odot)-44.0198(M/10\ {\rm M}_\odot)^2\\ +5.58876(M/10\ {\rm M}_\odot)^3-0.226361(M/10\ {\rm M}_\odot)^4\\ \qquad(20\ {\rm M}_\odot\leqslant M\leqslant100\ {\rm M}_\odot).\end{cases}\tag{16}$$

The green line in Fig. 3 shows the rms error of our fitting formula in the He-burning phase. We find that our fitting formula for each mass has accuracies within 6% of the stellar models of Marigo et al. (2001) during this phase.

In the He-burning phase, a star evolves into a giant star, which has the core-envelope structure. The structure can be characterized by the He-core mass at the beginning and the end of the He-burning. These core masses are approximated by

$$(M^{\rm b}_{\rm He}/{\rm M}_\odot)=\begin{cases}-0.47466+2.49981(M/10\ {\rm M}_\odot)^{1.13274}\\ \qquad(10\ {\rm M}_\odot\leqslant M<15\ {\rm M}_\odot),\\ -2.3546+3.61261(M/10\ {\rm M}_\odot)^{1.12392}\\ \qquad(15\ {\rm M}_\odot\leqslant M\leqslant100\ {\rm M}_\odot),\end{cases}\tag{17}$$

and

$$(M^{\rm e}_{\rm He}/{\rm M}_\odot)=1.31569(M/10\ {\rm M}_\odot)+0.993475(M/10\ {\rm M}_\odot)^2\\ -0.112405(M/10\ {\rm M}_\odot)^3+4.60669\times10^{-3}(M/10\ {\rm M}_\odot)^4.\tag{18}$$

Then, the He-core mass as a function of the total stellar mass and time can be given by

$$(M_{\rm He}/{\rm M}_\odot)=(M^{\rm b}_{\rm He}/{\rm M}_\odot)+A_{\rm He}\tau_{\rm He}+B_{\rm He}\tau^2_{\rm He}\\ +((M^{\rm e}_{\rm He}/{\rm M}_\odot)-(M^{\rm b}_{\rm He}/{\rm M}_\odot)-A_{\rm He}-B_{\rm He})\tau^3_{\rm He},\tag{19}$$

where

$$A_{\rm He}=\begin{cases}-301.285+1210.26(M/10\ {\rm M}_\odot)-1808.76(M/10\ {\rm M}_\odot)^2\\ +1191.99(M/10\ {\rm M}_\odot)^3-292.114(M/10\ {\rm M}_\odot)^4\\ \qquad(10\ {\rm M}_\odot\leqslant M<12\ {\rm M}_\odot),\\ -1.27007+2.97787(M/10\ {\rm M}_\odot)-1.66077(M/10\ {\rm M}_\odot)^2\\ +0.307506(M/10\ {\rm M}_\odot)^3\\ \qquad(12\ {\rm M}_\odot\leqslant M<30\ {\rm M}_\odot),\\ 5.55735\times10^{-2}-4.91742\times10^{-2}(M/10\ {\rm M}_\odot)\\ +9.62294\times10^{-2}(M/10\ {\rm M}_\odot)^2\\ -9.4471\times10^{-3}(M/10\ {\rm M}_\odot)^3\\ \qquad(30\ {\rm M}_\odot\leqslant M\leqslant100\ {\rm M}_\odot),\end{cases}\tag{20}$$

and

$$B_{\rm He}=\begin{cases}20.771-47.8361(M/10\ {\rm M}_\odot)+38.9548(M/10\ {\rm M}_\odot)^2\\ -13.6227(M/10\ {\rm M}_\odot)^3+1.70524(M/10\ {\rm M}_\odot)^4\\ \qquad(10\ {\rm M}_\odot\leqslant M<30\ {\rm M}_\odot),\\ -9.30219+4.79562(M/10\ {\rm M}_\odot)\\ -0.937401(M/10\ {\rm M}_\odot)^2\\ +5.62695\times10^{-2}(M/10\ {\rm M}_\odot)^3\\ \qquad(30\ {\rm M}_\odot\leqslant M\leqslant100\ {\rm M}_\odot).\end{cases}\tag{21}$$

(3) He-shell burning phase

After the He-burning ends in the core, the He-shell burning starts until the onset of the C-burning. The He-shell burning phase is characterized by the stellar radius at the end of the He-burning $R^{\rm e}_{\rm He}$, the stellar radius at the beginning of the C-burning $R^{\rm b}_{\rm C}$, and the ignition time of the C-burning $t^{\rm b}_{\rm C}$.

$R_{\rm C}^{\rm b}$ and $t_{\rm C}^{\rm b}$ are approximated by

$$\log(R_{\rm C}^{\rm b}/{\rm R}_\odot) = \begin{cases} 5.4491 - 5.78767(M/10\ {\rm M}_\odot) \\ +1.99667(M/10\ {\rm M}_\odot)^2 \\ \qquad (10\ {\rm M}_\odot \leqslant M < 15\ {\rm M}_\odot), \\ 1.39753 - 0.254317(M/10\ {\rm M}_\odot) \\ +0.106221(M/10\ {\rm M}_\odot)^2 \\ \qquad (15\ {\rm M}_\odot \leqslant M \leqslant 50\ {\rm M}_\odot) \\ 0.51943 + 0.621622(M/10\ {\rm M}_\odot) \\ -3.48026\times10^{-2}(M/10\ {\rm M}_\odot)^2 \\ \qquad (50\ {\rm M}_\odot \leqslant M \leqslant 100\ {\rm M}_\odot), \end{cases} \tag{22}$$

and

$$(t_{\rm C}^{\rm b}/{\rm Myr}) = 2.09464 + \frac{106.25}{10(M/10\ {\rm M}_\odot) - 3.90499}, \tag{23}$$

respectively. Then, using the normalized time which is defined by

$$\tau_{\rm HeS} \equiv \frac{t - t_{\rm H} - t_{\rm He}}{t_{\rm C}^{\rm b} - t_{\rm H} - t_{\rm He}}, \tag{24}$$

the fitting formula of the stellar radius at the He-shell burning phase is obtained as

$$\log(R_{\rm HeS}/{\rm R}_\odot) = \begin{cases} \log(R_{\rm He}^e/{\rm R}_\odot) + a_{\rm HeS}\tau_{\rm HeS} + b_{\rm HeS}\tau_{\rm HeS}^2 \\ +c_{\rm HeS}\tau_{\rm HeS}^3 + (\log(R_{\rm C}^{\rm b}/R_{\rm He}^e) \\ -a_{\rm HeS} - b_{\rm HeS} - c_{\rm HeS})\tau_{\rm HeS}^{15} \\ \qquad (10\ {\rm M}_\odot \leqslant {\rm M} \leqslant 50\ {\rm M}_\odot), \\ \log(R_{\rm He}^e/{\rm R}_\odot) + \log(R_{\rm C}^{\rm b}/R_{\rm He}^e)\tau_{\rm HeS} \\ \qquad (50\ {\rm M}_\odot < {\rm M} \leqslant 100\ {\rm M}_\odot), \end{cases} \tag{25}$$

where

$$a_{\rm HeS} = \begin{cases} 0.198773 - 8.62031\times10^{-2}(M/10\ {\rm M}_\odot) \\ -6.9987\times10^{-2}(M/10\ {\rm M}_\odot)^2 \\ \qquad (10\ {\rm M}_\odot \leqslant M < 15\ {\rm M}_\odot), \\ -2.17094 + 2.46127(M/10\ {\rm M}_\odot) \\ -0.866681(M/10\ {\rm M}_\odot)^2 \\ +9.41554\times10^{-2}(M/10\ {\rm M}_\odot)^3 \\ \qquad (15\ {\rm M}_\odot \leqslant M \leqslant 50\ {\rm M}_\odot), \end{cases} \tag{26}$$

$$b_{\rm HeS} = \begin{cases} 0.45 \quad (10\ {\rm M}_\odot \leqslant M < 15\ {\rm M}_\odot), \\ 5.85223 - 5.9911(M/10\ {\rm M}_\odot) + 2.05449(M/10\ {\rm M}_\odot)^2 \\ -0.217241(M/10\ {\rm M}_\odot)^3 \\ \qquad (15\ {\rm M}_\odot \leqslant M \leqslant 50\ {\rm M}_\odot), \end{cases} \tag{27}$$

and

$$c_{\rm HeS} = \begin{cases} 0.15 \quad (10\ {\rm M}_\odot \leqslant M < 15\ {\rm M}_\odot), \\ -2.34416 + 2.5736(M/10\ {\rm M}_\odot) - 0.920019(M/10\ {\rm M}_\odot)^2 \\ +0.100612(M/10\ {\rm M}_\odot)^3 \\ \qquad (15\ {\rm M}_\odot \leqslant M \leqslant 50\ {\rm M}_\odot), \end{cases} \tag{28}$$

The rms error in this phase is shown with the blue line in Fig. 3. We find that our fitting formula has an accuracy within 3.5 % of the stellar models of Marigo et al. (2001).

During the He-shell burning phase, we suppose that the CO-core mass, which is formed in the He-burning phase, remains constant. This is because the duration of the He-shell burning is so short that the CO-core mass does not change so much by the end of the He-shell burning.

For later use, we fit the stellar luminosity at the beginning of He-shell burning as

$$\begin{aligned} \log\left(\frac{L}{{\rm L}_\odot}\right) =& 6.74298 - 4.72995/(M/10\ {\rm M}_\odot) \\ &+ 3.59526/(M/10\ {\rm M}_\odot)^2 - 1.27068/(M/10\ {\rm M}_\odot)^3. \end{aligned} \tag{29}$$

For simplicity, we assume that the luminosity does not depend on time after the He-shell burning phase, because the luminosity is almost constant at this phase (see Figure 1).

(4) Compact remnants

After the C-ignition, the nuclear fusion further proceeds in the core and finally the Fe-Ni core is formed. The final fate of a star depends on the Fe-Ni core mass. However, at the C-ignition, we stop to trace the stellar evolution and regard the star to be a compact object, since the evolution time of the final stage is so short that the whole stellar structure hardly changes (Kippenhahn & Weigert 1990). From the numerical results of Pop III single stellar evolution, the CO-core mass is described as a function of the stellar mass as

$$\begin{aligned} (M_{\rm CO}/{\rm M}_\odot) =& 0.618397 - 0.57395(M/10\ {\rm M}_\odot) \\ &+ 1.73053(M/10\ {\rm M}_\odot)^2 - 0.312008(M/10\ {\rm M}_\odot)^3 \\ &+ 2.99858\times10^{-2}(M/10\ {\rm M}_\odot)^4 \\ &- 1.12942\times10^{-3}(M/10\ {\rm M}_\odot)^5. \end{aligned} \tag{30}$$

From the CO core mass, we can estimate the Fe-Ni core mass using the fitting formula given by Belczynski, Kalogera & Bulik (2002) as,

$$M_{\rm FeNi} = \begin{cases} 0.161767M_{\rm CO} + 1.067055\ {\rm M}_\odot & (M_{\rm CO} \leqslant 2.5\ {\rm M}_\odot), \\ 0.314154M_{\rm CO} + 0.686088\ {\rm M}_\odot & (2.5\ {\rm M}_\odot \leqslant M_{\rm CO}). \end{cases} \tag{31}$$

As for the criterion of whether a supernova explosion occurs or not after the stellar death, we here adopt the model adopted in Belczynski, Kalogera & Bulik (2002). The assumptions of the model is as follows: (1) supernovae can occur for stars with $M_{\rm CO} \leqslant 5\ {\rm M}_\odot$, (2) some fractions of envelope fall back onto the compact remnant after a supernova explosion for stars with the intermediate mass range of $5\ {\rm M}_\odot < M_{\rm CO} \leqslant 7.6\ {\rm M}_\odot$, (3) a star directly collapses so that a supernova explosion does not occur for a star with mass of $M_{\rm CO} > 7.6\ {\rm M}_\odot$. The remnant mass of the compact object in their model is given by

$$M_{\rm rem} = \begin{cases} M_{\rm FeNi} & (M_{\rm CO} \leqslant 5\ {\rm M}_\odot), \\ M_{\rm FeNi} + \frac{M_{\rm CO} - 5{\rm M}_\odot}{2.6{\rm M}_\odot}(M - M_{\rm FeNi}), & \\ & (5\ {\rm M}_\odot < M_{\rm CO} < 7.6\ {\rm M}_\odot), \\ M & (7.6\ {\rm M}_\odot \leqslant M_{\rm CO}). \end{cases} \tag{32}$$

From the value of a remnant mass, we determine the

type of a compact object, i.e., a neutron star or a black hole. We assume that the maximum mass of the neutron star is 3 $M_\odot$, which is higher than the mass of the observed massive pulsars $\sim 2M_\odot$. Thus a remnant is regarded as a black hole if its mass is higher than 3 $M_\odot$. Although the stellar evolution after the CO burning has been well studied (Woosley 1986; Timmes, Woosley & Weaver 1996; Fryer 1999; Fryer et al. 2012), there are uncertainties for the formation of a compact object. In particular, the mechanism of supernova explosions has not been theoretically established. Thus, our results might change depending on the models for supernova explosions. In this paper, we employ the same condition of the formation of a compact object as the previous studies (Belczynski, Kalogera & Bulik 2002; Belczynski, Bulik & Rudak 2004).

2.2 Binary evolution

For the calculation of binary stellar evolution, we need to consider binary interactions such as tidal evolution, mass transfer, effect of supernova explosions, and the radiation reaction by the gravitational wave. Here magnetic braking is not taken into account, because Pop III stars are expected to have magnetic fields much weaker than those of Pop I stars (e.g., Pudritz & Silk 1989; Kulsrud et al. 1997; Langer et al. 2003; Widrow 2002; Doi & Susa 2011).

2.2.1 Tidal evolution

The orbital angular momentum of a binary system $J_{\rm orb}$ is effectively transferred to the spin angular momentum $J_{\rm spin,i}$ through tidal interaction between the two stars. Here $i = 1$ and $i = 2$ correspond to the primary star with the mass of M_1 and the secondary star with the mass of M_2, respectively. The time variation of the parameters of a binary orbit such as the semi-major axis a, eccentricity e, $J_{\rm orb}$, and $J_{\rm spin,i}$ are given by Hurley, Tout & Pols (2002) as follows. The time variation of a is given by

$$\frac{\dot{a}}{a} = \frac{2e\dot{e}}{1-e^2} + 2\frac{\dot{J}_{\rm orb}}{J_{\rm orb}}. \tag{33}$$

Since the total angular momentum ($= J_{\rm orb} + J_{\rm spin,1} + J_{\rm spin,2}$) is conserved, $\dot{J}_{\rm orb}$ is given by $\dot{J}_{\rm orb} = -(\dot{J}_{\rm spin,1} + \dot{J}_{\rm spin,2})$. Denoting I_i and $\Omega_{\rm spin,i}$ as the moment of the inertia and the spin angular velocity of each star, $\dot{J}_{\rm spin,i}$ can be written as

$$\dot{J}_{\rm spin,i} = \dot{I}_i \Omega_{\rm spin,i} + I_i \dot{\Omega}_{\rm spin,i}, \tag{34}$$

where the first term of r.h.s expresses the contribution of the change of the internal structure of the star i and the second term is due to the tidal force from the other star. Hut (1981) showed that the time evolution of the spin angular velocity can be calculated by

$$\dot{\Omega}_{\rm spin,1} = 3\frac{k}{T}\frac{q_2^2}{r_{\rm g}^2}\left(\frac{R_1}{a}\right)^6 \frac{\Omega_{\rm orb}}{(1-e^2)^6} \times \left[f_1(e^2) - (1-e^2)^{\frac{3}{2}} f_2(e^2)\frac{\Omega_{\rm spin,1}}{\Omega_{\rm orb}}\right], \tag{35}$$

$$f_1(e^2) = 1 + \frac{15}{2}e^2 + \frac{45}{8}e^4 + \frac{5}{16}e^6, \tag{36}$$

$$f_2(e^2) = 1 + 3e^2 + \frac{3}{8}e^4, \tag{37}$$

$$q_2 \equiv M_2/M_1, \tag{38}$$

where T, k, $r_{\rm g}$ and $\Omega_{\rm orb}$ are the tidal timescale, the apsidal motion constant of the primary star, the gyration radius which is defined by $\sqrt{I_1/M_1/R_1^2}$ and the orbital angular velocity, respectively. T, k, and $r_{\rm g}$ depend on the properties of the internal structure of the primary star and their specific forms are given later. The time evolution of $\dot{\Omega}_{\rm spin,2}$ is given by changing 1 to 2 and 2 to 1 in the above equations. Once T, k, $r_{\rm g}$, and the binary parameters are given, one can determine $\dot{J}_{\rm orb}$ from $\dot{J}_{\rm spin,1} + \dot{J}_{\rm spin,2}$.

Hut (1981) also gave the equations for $\dot{e}$ as

$$\dot{e} = -27\frac{k}{T}q_2(1+q_2)\left(\frac{R_1}{a}\right)^8 \frac{e}{(1-e^2)^{\frac{13}{2}}} \times \left[f_3(e^2) - \frac{11}{18}(1-e^2)^{\frac{3}{2}} f_4(e^2)\frac{\Omega_{\rm spin,1}}{\Omega_{\rm orb}}\right], \tag{39}$$

$$f_3(e^2) = 1 + \frac{15}{4}e^2 + \frac{15}{8}e^4 + \frac{5}{64}e^6, \tag{40}$$

$$f_4(e^2) = 1 + \frac{3}{2}e^2 + \frac{1}{8}e^4. \tag{41}$$

Substituting Eqs. (34)–(41) into r.h.s of Eq. (33), we can determine the time evolution of the semi major axis a .

The moment of inertia I_i depends on the stellar evolutionary phase. I_i at H-burning phase can be written as $I_i = k_{\rm H}(M_i, \tau_{\rm H}) M_i R_i^2$. Hurley, Tout & Pols (2002) constructed a fitting formula of $k_{\rm H}(M_i, \tau_{\rm H})$ in their open code so that we adopt the same formula. On the other hand, when a star has core-envelope structure, $I_i = k_{\rm env}(M_i - M_{{\rm c},i})R_i^2 + k_{\rm core}M_{{\rm c},i}R_{{\rm c},i}^2$ (Hurley, Pols & Tout 2000; Hurley, Tout & Pols 2002), where $M_{{\rm c},i}$ and $R_{{\rm c},i}$ are the stellar core mass and radius, and $k_{\rm env}$ which is the same as $k_{\rm H}(M_i, \tau_{\rm H})$ in Hurley's open code and $k_{\rm core} = 0.21$, respectively. In this paper, we approximate the core radius using the core mass following Tout et al. (1997) as

$$\frac{R_{{\rm c},i}}{\rm R_\odot} = 0.9334\left(\frac{M_{{\rm c},i}}{10\ \rm M_\odot}\right)^{0.62}, \tag{42}$$

where the core mass corresponds to the He-core mass for a star with H-envelope and a CO-core mass for a star without H-envelope due to the binary interaction so-called naked-He star, respectively.

As for the initial stellar spin at the ZAMS phase, we follow Hurley, Pols & Tout (2000) as

$$\Omega_{{\rm spin},i} = 45.35\left(\frac{v_{\rm rot}}{1\ \rm km\ s^{-1}}\right)\left(\frac{R_{\rm ZAMS}}{\rm R_\odot}\right)^{-1}\ \rm yr^{-1}, \tag{43}$$

$$v_{\rm rot}(M_i) = \frac{658437(M_i/10\ \rm M_\odot)^{3.3}}{15 + 2818(M_i/10\ \rm M_\odot)^{3.45}}\ \rm km\ s^{-1}. \tag{44}$$

Next, we argue the apsidal motion constant k and tidal

time scale T. In the case that the primary envelope is convective, the energy dissipation due to the convective motions causes the lag of the tidal deformation, which yields the misalignment of the direction of the maximum tidal deformation and the direction to the secondary star. This misalignment generates the torque to the primary star so that the angular momentum is transferred between the spin one and the orbital one. According to Verbunt & Phinney (1995); Rasio et al. (1996), the apsidal motion constant decided by the tidal time scale for the convective envelope is given by

$$\frac{k}{T} = \frac{2}{21}\frac{f_{\rm con}}{\tau_{\rm con}}\frac{M_{\rm env,1}}{M_1}, \tag{45}$$

where $M_{\rm env,1} \equiv M_1 - M_{\rm c,1}$ is the primary envelope mass and the factor $f_{\rm con}$ is the correction of the tidal torque. The eddy turnover timescale $\tau_{\rm con}$, which describes the contribution of the turbulent viscosity due to the convective motions, is given by Hurley, Tout & Pols (2002),

$$\tau_{\rm con} = \left[\frac{M_{\rm env,1}R_{\rm env,1}\left(R_1 - \frac{1}{2}R_{\rm env,1}\right)}{3L_1}\right]^{1/3}, \tag{46}$$

where L_1 and $R_{\rm env,1} \equiv R_1 - R_{\rm c,1}$ are the stellar luminosity and the envelope radius of the primary star, respectively. If $\tau_{\rm con} \ll P_{\rm tid}/2$ $(= \pi|\Omega_{\rm orb} - \Omega_{\rm spin1}|^{-1})$, the turbulent viscosity due to the convective motions can be affected. If $\tau_{\rm con} > P_{\rm tid}/2$, on the other hand, the contribution of the convective motions to the viscosity is negligible. The factor $f_{\rm con}$ is obtained by Rasio et al. (1996) as

$$f_{\rm con} = \min\left[1, \left(\frac{P_{\rm tid}}{2\tau_{\rm con}}\right)^2\right]. \tag{47}$$

If the envelope is radiative, a tide is a dynamical tide with radiative damping (Zahn 1975). For a star which has the radiative envelope, the energy dissipation due to radiation is so small that the equilibrium tide cannot be effective. However, the non-radial oscillations at the surface are driven by gravity waves due to the tide and the resonances of those oscillations are damped by radiation. The value of k devided by T is given by Zahn (1977); Hurley, Tout & Pols (2002) as

$$\begin{aligned}\frac{k}{T} =& 4.3118\times10^{-8}\left(\frac{M_1}{\rm M_\odot}\right)\left(\frac{R_1}{\rm R_\odot}\right)^2 \\ &\times\left(\frac{a}{1\ {\rm AU}}\right)^{-5}(1+q_2)^{5/6}E\ {\rm yr}^{-1},\end{aligned} \tag{48}$$

where the tidal coefficient E is described by Zahn (1975) as

$$E = 1.101\times10^{-6}\left(\frac{M_1}{10\ {\rm M_\odot}}\right)^{2.84}. \tag{49}$$

2.2.2 Roche lobe overflow

When the primary star in a binary system fills its Roche lobe, its stellar envelope is transferred to the secondary star, which is called the Roche lobe overflow (RLOF). The radius of the Roche lobe of the primary star ($R_{\rm L,1}$) is approximately given by Eggleton (1983) as

$$\frac{R_{\rm L,1}}{a} \approx \frac{0.49q_1^{2/3}}{0.6q_1^{2/3} + \ln(1+q_1^{1/3})}, \tag{50}$$

where $q_1 \equiv M_1/M_2$ is the mass ratio. This equation is within 1% accuracy over the whole range. When the RLOF occurs and the primary star loses its envelope, the stellar radius changes depending on the properties of the stellar envelope (Paczyński & Sienkiewicz 1972). Since the dynamical time of the star given by

$$\tau_{\rm dyn,1} = \frac{\pi}{2}\left(\frac{R_1^3}{2GM_1}\right)^{1/2} \tag{51}$$

is much shorter than the thermal timescale (Kelvin-Helmholtz timescale) given by

$$\tau_{\rm KH,1} = \frac{GM_1(M_1 - M_{\rm c,1})}{L_1R_1}, \tag{52}$$

the radius of the primary star after the mass transfer is adjusted to *the adiabatic radius* $R_{\rm ad,1}$ first, that is, the star reaches the hydrostatic equilibrium state but not the thermal equilibrium. After the thermal time scale, the primary radius approaches *the thermal equilibrium radius* $R_{\rm th,1}$. The mass transfer via the RLOF actually depends on the responses of the Roche lobe radius, $R_{\rm ad,1}$ and $R_{\rm th,1}$ after the mass transfer.

We here introduce the following two quantities for convenience to understand the fate of the binary after the RLOF;

$$\zeta_{\rm L} = \frac{d\log R_{\rm L,1}}{d\log M_1}, \tag{53}$$

and

$$\zeta_{\rm ad} = \frac{d\log R_{\rm ad,1}}{d\log M_1}. \tag{54}$$

Since it is difficult to obtain the exact forms $\zeta_{\rm L}$ and $\zeta_{\rm ad}$, we here use the approximated expressions. Assuming that the mass transfer is conservative i.e., the total mass is conserved during the mass transfer, we have $\zeta_{\rm L}$ as (Tout et al. 1997)

$$\zeta_{\rm L} \approx 2.13q_1 - 1.67 \quad (0 < q_1 < 50), \tag{55}$$

where we use Eq. (50). The value of $\zeta_{\rm ad}$ depends on the property of the stellar envelope. When the primary star is in the giant phase, it has a deep convective envelope with the polytropic index of 1.5 so that $\zeta_{\rm ad}$ is given by

$$\zeta_{\rm ad} \approx -1 + \frac{2}{3}\frac{M_1}{M_1 - M_{c1}}, \tag{56}$$

under the assumption that the envelope mass is neglected compared to the total mass (Hjellming & Webbink 1987). When the primary star is in the other stages, $\zeta_{\rm ad} = 2.59, 6.85, 1.95$ and 5.79 for the main sequence, the giant phase with the radiative envelope (Hjellming 1989), the naked-He main sequence and the naked-He giant star (Ivanova, Podsiadlowski & Spruit 2002; Belczynski et al. 2008), respectively.

Now let us compare $\zeta_{\rm ad}$ and $\zeta_{\rm L}$. We first consider the case of $\zeta_{\rm ad} < \zeta_{\rm L}$, which means $d\log R_{\rm ad,1} > d\log R_{\rm L,1}$ since $d\log M_1 < 0$. In this case, the radius of the primary star continues to exceed the Roche lobe radius at the dynamical timescale as the primary star loses its envelope. Thus, the mass transfer violently occurs and the stars rapidly approach

each other [7]. When the primary star is a giant with the outer envelope, which is either radiative or convective, the primary envelope rapidly swallows the secondary star. After that, the binary stars will be in the common envelope (CE) phase (Paczynski 1976). We describe the subsequent evolution of the binary in Sec. 2.2.3. On the other hand, when the primary star does not have the core-envelope structure like in the H-burning main sequence and naked-He main sequence, the binary will merge via the rapid mass transfer.

Next, we consider the case for $\zeta_{\rm ad} > \zeta_{\rm L}$. In this case, the primary star shrinks within the Roche lobe radius ($R_{\rm ad,1} < R_{\rm L,1}$) on the dynamical timescale by the mass transfer of the envelope so that RLOF stops for a while. However in the thermal timescale, the radius of the primary star approaches $R_{\rm th,1}$. If the thermal equilibrium radius is larger than the Roche lobe radius, the mass transfer begins and the transfer rate is expressed by Paczyński & Sienkiewicz (1972); Tout et al. (1997); Hurley, Tout & Pols (2002) as

$$\dot{M}_1 = F(M_1)\left[\ln\left(\frac{R_{\rm th,1}}{R_{\rm L,1}}\right)\right]^3 \ {\rm M}_\odot \ {\rm yr}^{-1} \tag{57}$$

and

$$F(M_1) = 3\times10^{-6}\left\{\min\left[\left(10\frac{M_1}{10\ {\rm M}_\odot}\right), 5.0\right]\right\}^2, \tag{58}$$

where the expression of $R_{\rm th,1}$ is shown in Appendix A.1. Since the stellar radius changes on the thermal timescale (or more slowly), the maximum value of the mass transfer rate is

$$\dot{M}_{1,\rm max} = \frac{M_1}{\tau_{\rm KH,1}}. \tag{59}$$

We assume that the binary stars merge if $R_{\rm th,1} > 10R_{\rm L,1}$ for the star without the core-envelope structure since the mass transfer rate is comparable to the above upper limit.

In the case of the stable mass transfer ($\zeta_{\rm ad} > \zeta_{\rm L}$), the accretion rate onto the secondary varies with its evolutionary stage (Hurley, Tout & Pols 2002). If the secondary is in the main sequence or in the He-burning phase, the accretion timescale

$$\tau_{\dot{M}} \equiv \frac{M_2}{\dot{M}_1} \tag{60}$$

is much shorter than the thermal timescale of the secondary $\tau_{\rm KH,2}$. Therefore the secondary does not always receive all the accreting matter, and the accretion rate onto the secondary is calculated by (Hurley, Tout & Pols 2002) as

$$\dot{M}_2 = \min\left(10\frac{\tau_{\dot{M}}}{\tau_{\rm KH,2}}, 1\right)\dot{M}_1. \tag{61}$$

If the secondary is in the He-shell burning phase or the naked-He star, the secondary can receive all the accreting mass (Hurley, Tout & Pols 2002). For the secondary of the compact object, the accretion rate is limited by the Eddington limit (Cameron 1967; Hurley, Tout & Pols 2002) as

$$\dot{M}_{\rm Edd} = \frac{4\pi cR_2}{\kappa_{\rm T}} = 2.08\times10^{-3}(1+X)^{-1}\left(\frac{R_2}{\rm R_\odot}\right)\ {\rm M}_\odot\ {\rm yr}^{-1}, \tag{62}$$

where $\kappa_{\rm T} = 0.2(1+X)$ cm^2 g^{-1} is the opacity of the Thomson scattering and $X(=0.76)$ is the H-mass fraction.

[7] For simplicity, we here assume the conservation of the angular momentum and neglect the mass ejection from the binary system during the mass transfer on the dynamical timescale.

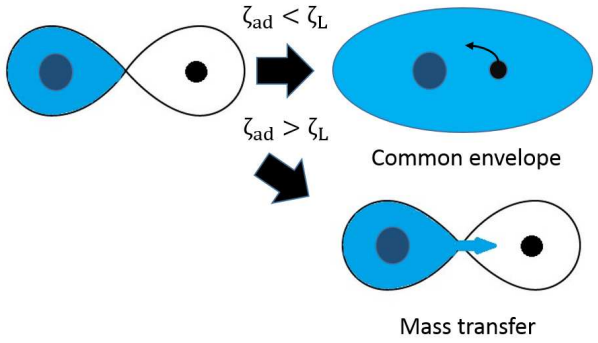

Figure 4. Schematic diagram of the mass transfer when the primary becomes a giant star. Let us define $\zeta_{\rm L} = d\log R_{\rm L,1}/d\log M_1$ and $\zeta_{\rm ad} = d\log R_{\rm ad,1}/d\log M_1$. When the primary star fulfills the Roche lobe as in the upper left of the figure, there are two destinies. 1) If $\zeta_{\rm ad} < \zeta_{\rm L}$, then $d\log R_{\rm ad,1} > d\log R_{\rm L,1}$ since $d\log M_1 < 0$ so that the mass transfer is dynamically unstable. The secondary star is swallowed by the primary envelope to be the common envelope phase as the upper right of the figure. 2) If $\zeta_{\rm ad} > \zeta_{\rm L}$, the mass transfer is dynamically stable so that the radius of the primary star becomes smaller than the Roche lobe radius on the dynamical timescale after losing the small fraction of the envelope mass. However in the thermal time scale (Kelvin-Helmholz time), the radius increases again and fulfills the Roche lobe so that the stable mass transfer from the primary star to the secondary star occurs like in the lower right of the figure.

2.2.3 Common envelope phase

If $\zeta_{\rm ad} < \zeta_{\rm L}$, the mass transfer occurs violently from the primary star with the core-envelope structure to the secondary so that the binary system becomes the CE phase as discussed in the previous Sec. 2.2.2. Once the secondary star is engulfed into the primary envelope, it spirals into the core of the primary star due to the gas friction. Then, the orbital energy is converted into the thermal energy of the primary envelope, which results in the mass ejection from the binary system. As we showed in Sec. 2.2.2, stars with convective envelope typically take smaller values of $\zeta_{\rm ad}$ than stars with radiative envelope. Thus the former stars are easier to satisfy the condition of the onset of the CE phase of $\zeta_{\rm ad} < \zeta_{\rm L}$ than the latter ones. For Pop III stars, we determine whether they have the radiative or convective envelope from the HR diagram in Fig. 1. We found that Pop III stars with mass $\geqslant 70$ M$_\odot$ reach the Hayashi track at the beginning of the He-shell burning. While Pop III stars less massive than 50 M$_\odot$ do not reach the Hayashi track. Thus, Pop III stars with

mass > 50 M$_\odot$ develop the deep convective envelope during the He-shell burning phase and are easier to be the CE phase.

In order to take into account the CE phase, we here adopt the prescription given by Webbink (1984). For simplicity, we assume that all gas in the primary envelope is ejected. Then, the change of the orbital energy when the secondary star spirals in is expressed as

$$\Delta E_{\rm orb} = \frac{GM_{\rm c,1}M_2}{2a_{\rm f}} - \frac{GM_1M_2}{2a_{\rm i}}, \tag{63}$$

where $a_{\rm i}$ and $a_{\rm f}$ are the separation before and after the secondary star spirals in, respectively. A fraction of the orbital energy is actually converted to the kinetic energy of the ejected matter. The binding energy of the primary envelope is somewhat smaller than the gravitational energy, and thus, it is expressed by

$$E_{\rm bind} = \frac{GM_1M_{\rm env,1}}{\lambda R_1}, \tag{64}$$

where λ is a parameter depending on the properties of the envelope and $M_{\rm env,1}$ is the mass of the primary envelope. Therefore, we can estimate the final separation $a_{\rm f}$ by

$$\alpha\left(\frac{GM_{\rm c,1}M_2}{2a_{\rm f}} - \frac{GM_1M_2}{2a_{\rm i}}\right) = \frac{GM_1M_{\rm env,1}}{\lambda R_1}, \tag{65}$$

where α is the efficiency factor of the energy conversion which depends on the interaction between the primary envelope and the secondary star. When the secondary star is also a giant star, we need to modify the above prescription. For simplicity, we assume that the remnants after the mass ejection are two cores and the values of the λ parameter are the same for both envelopes. Then, we can obtain the final separation $a_{\rm f}$ from

$$\alpha\left(\frac{GM_{\rm c,1}M_{\rm c,2}}{2a_{\rm f}} - \frac{GM_1M_2}{2a_{\rm i}}\right) = \frac{GM_1M_{\rm env,1}}{\lambda R_1} + \frac{GM_2M_{\rm env,2}}{\lambda R_2}. \tag{66}$$

To determine the values of α and λ, the sophisticated numerical simulations including the hydrodynamics in the CE phase and the stellar evolution are required (Xu & Li 2010; Loveridge, van der Sluys & Kalogera 2011). However, to do these simulations for each star is actually time consuming. So, in this paper, we assume $\alpha\lambda = 1$ as in the previous studies (Hurley, Tout & Pols 2002; Belczynski, Kalogera & Bulik 2002; Belczynski et al. 2008).

Next, we describe the treatment of the fate of the binary after the mass ejection at the CE phase. When the final separation estimated from Eqs. (65) or (66) is small, the binary will merge under following two conditions. The first condition is a simple one by Belczynski, Kalogera & Bulik (2002); Belczynski, Bulik & Rudak (2004); Belczynski et al. (2008); Dominik et al. (2012), where the core of the binary merges if $R_1' + R_2' > a_{\rm f}$. Since the binary merges in this case only if the binary stars contact each other, we call this condition as the *conservative core merger criterion*. The second condition is the same as that used in Hurley, Tout & Pols (2002), that is, if $R_1' > R_{\rm L,1}'$ or $R_2' > R_{\rm L,2}'$ where the quantities with prime mean the value after the mass ejection. In other words, this means that the cores of the binary stars merge if the mass transfer occurs during the CE phase. However, there are arguments against this by Ivanova, Podsiadlowski & Spruit (2002); Podsiadlowski et al. (2010) so that we call this condition as *optimistic core merger criterion* .

2.2.4 Effect of supernova explosion

When a supernova explosion occurs, binary parameters ($M_{\rm total} \equiv M_1 + M_2, a, e$) change due to the instant mass ejection and the kick velocity. In our present simulations, we assume zero kick velocity for simplicity. The neutron star formation with the kick velocity is easier to disrupt NS-NSs than the spherically symmetric supernova explosion so that the merger rate of NS-NSs and NS-BHs from our simulations should be considered as the upper limit. While in the formation of a black hole, zero kick velocity is reasonable so that the formation rate of BH-BHs is reliable.

Before the supernova explosion, the relative velocity $\mathbf{v}$ is described by the orbital speed v and the angle β between the relative velocity and the separation vector $\mathbf{r} \equiv \mathbf{r}_1 - \mathbf{r}_2$ as

$$\mathbf{v} = (-v\sin\beta, -v\cos\beta, 0), \tag{67}$$

where the orbital speed is expressed by the specific orbital energy $GM_{\rm total}/2a$ as

$$v = \sqrt{GM_{\rm total}\left(\frac{2}{r} - \frac{1}{a}\right)}, \tag{68}$$

where a is the semi major axis before the supernova explosion. After the supernova of the primary star, it ejects mass instantly is a good approximation since the expansion velocity of the supernova ejecta ($\sim 10^9$cm/s) is much larger than the orbital velocity. Thus, the total mass immediately after the supernova explosion is

$$M_{\rm total} \to M_{\rm total}' = M_{\rm total} - \Delta M_1 \tag{69}$$

where the subscript ' means the value immediately after the supernova explosion and ΔM_1 is the primary ejected mass. The relative velocity immediately after the supernova explosion is described by

$$v' = \sqrt{GM_{\rm total}'\left(\frac{2}{r} - \frac{1}{a'}\right)}. \tag{70}$$

The relative velocity does not change immediately after the supernova explosion, because the spherically symmetric supernova explosion does not change the specific angular momentum. Thus, $v = v'$. Therefore, using the equation (68) and (70), we have the separation after supernova explosion as

$$a' = \left(\frac{v^2}{GM_{\rm total}} - \frac{v^2}{GM_{\rm total}'} + \frac{1}{a}\right)^{-1}. \tag{71}$$

The eccentricity after the supernova explosion is calculated by the conservation of the specific angular momentum as

$$e' = \sqrt{1 - \frac{|\mathbf{r}\times\mathbf{v}|^2}{GM_{\rm total}'a'}}. \tag{72}$$

For example, let us consider the case of the initial $e = 0$. In this case, $r = a$ and $v = (GM_{\rm total}/a)^{1/2}$. Thus, the separation and the eccentricity after the supernova explosion are

$$a' = \left(\frac{2}{a} - \frac{M_{\rm total}}{M'_{\rm total}a}\right)^{-1}, \tag{73}$$

$$e' = \frac{M_{\rm total}}{M'_{\rm total}} - 1. \tag{74}$$

The mass ejection of the supernova explosion decelerates the escape velocity of the binary. On the other hand, the velocity of compact object in the supernova remnant does not change. Thus, if the mass ejection is lager than a half of the total mass of the binary, the velocity of the compact object can be larger than the escape velocity. Therefore, if $M'_{\rm total} < \frac{1}{2}M_{\rm total}$, the binary is disrupted.

Note that in Hurley's original code, when the supernova explosion occurs as soon as after the CE phase, the primary mass before the CE phase is treated as the primary mass before the supernova explosion. On the other hand, we assume that the primary mass after the CE phase is treated as the primary mass before the supernova explosion.

2.2.5 Coalescence time due to the emission of gravitational waves

When the stars of a binary system explode or collapse at the end of their lifetime, the compact star binary is formed. The compact binary loses the angular momentum and the orbital energy by the emission of gravitational waves. We use the slow-motion and weak-field approximation formalism described by Peters & Mathews (1963) and Peters (1964). The equations of the change of the angular momentum, the semi major axis and the eccentricity are given by

$$\frac{\dot{J}}{J} = -\frac{32G^3M_1M_2M_{\rm total}}{5c^5a^4}\frac{1+\frac{7}{8}e^2}{(1-e^2)^{5/2}}, \tag{75}$$

$$\frac{\dot{a}}{a} = -\frac{64G^3M_1M_2M_{\rm total}}{5c^5a^4}\frac{1+\frac{73}{24}e^2+\frac{37}{96}e^4}{(1-e^2)^{7/2}}, \tag{76}$$

and

$$\frac{\dot{e}}{e} = -\frac{304G^3M_1M_2M_{\rm total}}{15c^5a^4}\frac{1+\frac{121}{304}e^2}{(1-e^2)^{5/2}}. \tag{77}$$

From Eqs. (76) and (77), we can express a by e as

$$\frac{a}{a_0} = \frac{1-e_0^2}{1-e^2}\left(\frac{e}{e_0}\right)^{12/19}\left(\frac{1+\frac{121}{304}e^2}{1+\frac{121}{304}e_0^2}\right)^{870/2299}, \tag{78}$$

where a_0 and e_0 are the initial values of a and e, respectively. For $a/a_0 \ll 1$, Eq. (78) is approximated by

$$e \sim \left(\frac{a}{a_0(1-e_0^2)}\right)^{19/12}e_0. \tag{79}$$

For $e_0 = 0$, Eq. (76) is integrated as

$$t_{\rm coal}(e_0=0) = \frac{5}{256}\frac{a_0^4}{c}\left(\frac{GM_1}{c^2}\right)^{-1}\left(\frac{GM_2}{c^2}\right)^{-1}\left(\frac{GM_{\rm total}}{c^2}\right)^{-1} \tag{80}$$

$$= 10^{10}(\frac{a_0}{16\ {\rm R}_\odot})^4\left(\frac{M_1}{10\ {\rm M}_\odot}\right)^{-1}\left(\frac{M_2}{10\ {\rm M}_\odot}\right)^{-1}\left(\frac{M_{\rm total}}{10\ {\rm M}_\odot}\right)^{-1}\ {\rm yr}.$$

Peters & Mathews (1963) and Peters (1964) found numerically that for $e_0 > 0$, $t_{\rm merge}(e_0)$ is approximately given by

$$t_{\rm coal}(e_0) \sim (1-e_0^2)^{7/2}t_{\rm merge}(e_0=0). \tag{81}$$

However in our simulations, we solve Eqs. (75) and (77).

2.3 Initial condition

In this paper, we calculate the evolution of 10^6 binaries using the fitting formulae (see Sec. 2.1.2) and prescriptions for the binary interactions (see Sec. 2.2). As initial conditions, we should set the binary parameters, that is, the primary mass M_1, the mass ratio of secondary to primary $q_2 = M_2/M_1 < 1$ with M_2 being the secondary mass, the eccentricity e and the semi major axis a. In this section, we describe how to generate the initial conditions of 10^6 binaries.

2.3.1 Distribution function of the binary parameters

Since the distribution functions of the binary parameters are not known for Pop III stars, as a first step we use those of the observed Pop I stars except for the initial mass function (IMF).

(1) Initial mass

We consider two kinds of the IMF to study the dependence of the results on IMF. The first one is the Salpeter IMF (Salpeter 1955) given by

$$\Psi(M_1) \propto M_1^{-2.35}, \tag{82}$$

where $\Psi(M_1)$ is the number of stars per unit mass. The second one is the flat IMS given by

$$\Psi(M_1) \propto {\rm const.} \tag{83}$$

This mass function is suggested by some numerical simulations of the Pop III star formation(Clark, Glover & Simon et al. 2011). We set the mass range of $10\ {\rm M}_\odot \leqslant M_1 \leqslant 100\ {\rm M}_\odot$ to the mass of the primary star, as suggested by the recent numerical simulations (Hirano et al. 2013).

(2) Initial mass ratio

The distribution function of the initial mass ratio $q_2 < 1$ is given by

$$\Phi(q_2) \propto {\rm const.} \tag{84}$$

This distribution is suggested by the recent observations of binary systems (Kobulnicky & Fryer 2007; Kobulnicky et al. 2012). We set the minimum mass ratio to be $q_{2,\rm min} \equiv 10\ {\rm M}_\odot/M_1$, because we assume that the secondary mass range is the same as that of the primary.

(3) Initial eccentricity

Following Heggie (1975) and Duquennoy, Mayor & Halbwachs (1991), we use the distribution function of the initial eccentricity in the form of

$$\Xi(e) \propto e, \tag{85}$$

for the range of $0 \leqslant e \leqslant 1$.

(4) Initial separation

We adopt the logarithmically flat distribution for the initial semi major axis following Abt (1983) as

$$\Gamma(a) \propto \frac{1}{a}, \tag{86}$$

for the range of $A_{\rm min} \leqslant a \leqslant 10^6$ R$_\odot$. $A_{\rm min}$ is determined from Eq. (50) as

$$\begin{aligned} A_{\rm min} &= \frac{A_{\rm L}}{1-e} \\ &= \frac{0.6q_1^{2/3} + \ln(1+q_1^{1/3})}{0.49q_1^{2/3}} \frac{R_1}{1-e}. \end{aligned} \tag{87}$$

$A_{\rm L}$ corresponds to the separation when the primary star fills its Roche lobe at the peri-astron at the initial time. A binary should not fill its Roche lobe from the beginning so that we adopt this minimum separation.

2.3.2 Monte Calro method

We generate the initial conditions of binaries using the above distribution functions and the Monte Carlo method. In this paper, we mainly set the total number of binaries $N_{\rm total}$ to be 10^6. For example, we describe how to generate the initial condition of the primary mass. We prepare the homogeneous random variable X in the interval of $0 \leqslant X \leqslant 1$. For random choice of X, we define M_1 by

$$X \equiv \frac{\int_{M_{\rm min}}^{M_1} \Psi(M) dM}{\int_{M_{\rm min}}^{M_{\rm max}} \Psi(M) dM}. \tag{88}$$

For example in the case of the Salpeter IMF with the mass range of 10 M$_\odot \leqslant M_1 \leqslant$ 100 M$_\odot$, M_1 is given by

$$M_1 = [10^{-1.35} - X(10^{-1.35} - 100^{-1.35})]^{-1/1.35} \ {\rm M}_\odot. \tag{89}$$

We assign a random number generated by the Mersenne twister method (Matsumoto & Nishimura 1998) to the number X and set the primary mass M_1. For the other parameters (q_2, e, and a), we also generate the initial parameters in the same way. To check the reliability of our Monte Carlo method, in Appendix A.2, we perform the same simulations as Hurley, Tout & Pols (2002) and obtain the similar results. In Appendix A.3, we show the convergence check, that is, for one model, we performed the simulations with 10^5, 10^6 and 10^7 binaries. The results agree with each other within the statistical errors.

3 RESULTS

We compute the evolution of 10^6 binaries having random values of binary parameters. In this paper, we adopt the four models as shown in Table 1. Each column represents the name of the model, population of stars, IMF, mass range of the primary star, and that of the secondary star, respectively. Models III.s and III.f are simulations of Pop III binaries with the mass range of 10 M$_\odot \leqslant M \leqslant$ 100 M$_\odot$. For Models III.s and III.f, the Salpeter and flat IMF are adopted, respectively. Models I.h and I.l are simulations of Pop I binaries with Hurley's single stellar fitting formulae (Hurley, Pols & Tout 2000) for comparison. In both models, the Salpeter IMF is adopted. For Model I.h, the initial mass range is 10 M$_\odot \leqslant M \leqslant$ 100 M$_\odot$. For Model I.l, the initial mass range is 1 M$_\odot \leqslant M \leqslant$ 100 M$_\odot$ to take into account the typical mass of a Pop I star of $\sim$ 1M$_\odot$.

The number of the resulting compact binaries formed in each model is listed in Table 2. The numbers in the parenthesis are the numbers of the resulting compact binaries for the case of the conservative core merger criterion, which is mentioned in Sec. 2.2.3. In addition, the number of the compact binaries with coalescence time less than 15 Gyr is shown in Table 3. For compact binaries which merge within 15 Gyr, we show four tables and three figures to see more details for each model. In Tables 4, 5, 6 and 7, we describe the formation channels and the evolution histories of the compact binaries for each model. The abbreviated terms should be referred to the caption of Table 4. Figure 5 gives the distribution of the coalescence time, which is defined as the time between the birth of the binary and the merger. The normalization of the vertical axis is $dN/d\log t/N_{\rm total}$. Figures 6 and 7 are the distribution of the total mass ($M_{\rm tot} = M_1 + M_2$) and the chirp mass ($M_{\rm chirp} = (M_1 M_2)^{3/5}/(M_1+M_2)^{1/5}$) of the compact binaries, respectively.

3.1 Pop III compact binaries with the Salpeter IMF

We now discuss the evolution of Pop III binaries and their final fate in more detail. Here we focus on Model III.s as the reference model.

3.1.1 Binary black hole

From Tables 2 and 3, we find that $\sim$ 58 % of Pop III compact binaries are BH-BHs. Remarkably, $\sim$ 20 % of the BH-BHs merge within the age of the universe ($\sim$ 15 Gyr). The coalescence time of BH-BHs distributes almost uniformly and its value is $\sim$ 10-10^2 times larger than that of NS-BHs and NS-NSs (Fig. 5). The total and chirp mass distributions of the coalescing BH-BHs has a peak at $\sim$ 50 M$_\odot$ (Fig. 6) and $\sim$ 30 M$_\odot$ (Fig. 7), respectively. It is worth to note that more than $\sim$ 50% of these BH-BHs does not experience the CE phase (see Table 4) but RLOF. Therefore, we expect that the uncertainties of the parameters α and λ in the CE phase do not affect the major part of the PopIII BH-BH mergers.

3.1.2 Neutron star – black hole binaries

Although the total number of NS-BHs is comparable to that of BH-BH binaries, the number of the coalescing NS-BH within 15 Gyr is very small (Tables 2 and 3). Specifically, only 0.2 % of NS-BHs merges within 15 Gyr. In our results, the typical mass of a NS-BH is $(M_{\rm NS}, M_{\rm BH}) = (1.4\ {\rm M}_\odot, 30\ {\rm M}_\odot)$ and the typical separation is 10^4-10^6 $R_\odot$ so that the merging time is much larger than 15Gyr from Eq. (79). For NS-BH formation, the secondary star evolves into a neutron star via a supernova explosion after the formation of the black hole of the primary star. In order to follow this evolutionary path, the secondary should have mass less than ~ 50 $M_\odot$, otherwise the binary disrupts by the sudden mass loss at the supernova explosion. However such a star evolves via a blue supergiant (BSG) with the radiative envelope for the Pop III case (Fig. 1). Since a star with radiative envelope typically takes a larger value of $\zeta_{\rm ad}$ than those with convective envelope, such a star is more difficult to satisfy the condition of the onset of the CE phase ($\zeta_{\rm ad} < \zeta_{\rm L}$; Sec. 2.2.3). Therefore, Pop III binaries which form NS-BH tend to avoid the CE phase. As we described in Sec. 2.2.4, if the binary system ejects the mass comparable to half of the total mass at the moment of the secondary supernova explosion, the separation of the NS-BH is extremely widened. Thus, the coalescence time due to the emission of the gravitational wave tends to be so long that the NS-BHs seldom merge within 15 Gyr.

3.1.3 Binary neutron star

We find that the NS-NSs are rarely formed and merge within 15 Gyr (Tables 2 and 3). Most Pop III stars with mass $\sim 10-20$ $M_\odot$ evolve to NSs through the BSGs with radiative envelope. Thus, the Pop III binary which evolves to the NS-NSs hardly experiences the mass-losing processes in the CE phase. As a result, the binary is easily disrupted by ejecting more than half of the mass of the binary system at the moment of supernova explosions. In Table 3, there is a tiny number of NS-NSs. This comes from the rare binaries who experience common envelope due to the initial small separation.

3.2 Model comparisons

3.2.1 Pop III with different IMFs

From the first two rows of Tables 3, we see that the rarity of the NS-NSs and NS-BHs which merge within 15Gyr are similar for Model III.s and Model III.f. The reason is the same as we discussed in the previous subsection. On the other hand, for BH-BHs, these numbers are several times larger in the flat IMF case (Model III.f). This is because the number of massive progenitors forming BHs is larger in the flat IMF than that in the Salpeter IMF. This feature can also be seen in the distribution of the coalescence time, the total mass, and the chirp mass (Figs. 5–7). While the peak mass is the same between the two IMFs, the fraction of massive stars above the peak becomes larger in the flat IMF.

The formation channels of BH-BHs also reflect the difference of IMFs (See Table 4 and 5). Here, we focus on the channel BHBH1, which has nothing to do with the CE phase. In Model III.s, the channel BHBH1 occupies about 54 % of all, while in Model III.f, it does about 35 %. The reason is that the fraction of massive stars with $\gtrsim 50$ $M_\odot$, which evolve into red supergiants (RSG; Fig. 1), is larger in the flat IMF. Since the stars with convective envelope like RSGs have smaller values of $\zeta_{\rm ad}$ and are easier to satisfy the condition of the onset of the CE phase ($\zeta_{\rm ad} < \zeta_{\rm L}$; See Sec. 2.2.3).

Note that in our calculation, if the stellar mass exceeds 100 $M_\odot$, the binary evolution is stopped since the numerical results of Marigo et al. (2001), and thus, our fitting formulae are given for stars only up to 100 $M_\odot$. Therefore, for the binaries with $M_{\rm total} > 100$ $M_\odot$, our result is an underestimated one. We are planning to cover this mass range in future.

3.2.2 The differences between Pop III and Pop I

(1) Same initial mass range

The stellar evolution of Pop III stars is entirely different from that of Pop I stars as we describe in Sec. 2.1.1. In the Pop III case, stars more massive than $\gtrsim 50$ $M_\odot$ evolve into RSGs and those with $\lesssim 50$ $M_\odot$ evolve into BSGs with radiative envelope (Fig. 1). On the other hand, in the Pop I case all stars evolve into RSGs with deep convective envelope. Therefore, some fractions of Pop III binaries avoid the CE phase. Here, by comparing Models III.s and I.h, which have the same IMF and mass range, we clarify how the difference in stellar population affects the formation and coalescence of compact binaries. The clear differences between them can be seen in the distributions of the coalescence time, total mass, and chirp mass of compact binaries in Figs. 5–7. In particular, for Pop I, the number of the merging NS-NSs is the largest, while for Pop III, that of BH-BHs (Figs. 5–7).

First, we focus on NS-NSs. From Tables 2 and 3, in Model III.s, much smaller number of NS-NSs are formed and merge within 15 Gyr than those in Model I.h. This comes from the fact that Pop III binaries lose a smaller amount of mass from the system by the stellar wind and the mass ejection in the CE phase than Pop I. Therefore Pop III binaries are easier to be disrupted or separated further away by losing the mass of the system at supernova explosions.

Secondly, the number of NS-BHs formed in Model III.s is almost the same as that in Model I.h (Table 2). However, in Model III.s, the number of coalescing NS-BHs is much smaller than that in Model I.h (Table 3). The reason is the same as the NS-NS case: the major fractions of Pop III binaries are separated further away by ejecting some fraction of the mass from the system when the supernova explosion occurs in the secondary.

Thirdly, apart from the previous two cases, the number of coalescing BH-BHs in Model III.s is much larger than that in Model I.h (Table 3). The reason is as follows. Firstly, Pop III binaries which evolve into BH-BH binaries lose little mass from the system before the black hole formation and the resultant BH-BHs typically become more massive than

Table 1. The model description for the Monte Carlo simulations. Each column represents the name of the model, population of stars, IMF, mass range of the primary star and that of the secondary star, respectively. Models III.s and III.f are simulations of Pop III binaries with the mass range of 10 $M_\odot \leqslant M \leqslant 100$ $M_\odot$. For Models III.s and III.f, the Salpeter and flat IMF is adopetd, respectively. Models I.h and I.l are simulations of Pop I binaries with Hurley's single stellar fitting formulae (Hurley, Pols & Tout 2000) for comparison. In both models, the Salpeter IMF is adopted. For Model I.h, the initial mass range is 10 $M_\odot \leqslant M \leqslant 100$ $M_\odot$. For Model I.l, the initial mass range is 1 $M_\odot \leqslant M \leqslant 100$ $M_\odot$ to take into account the typical mass of a Pop I star is $\sim 1 M_\odot$.

model	population	IMF	primary mass range	secondary mass range
III.s	III	Salpeter	10 $M_\odot \leqslant M_1 \leqslant 100$ $M_\odot$	10 $M_\odot \leqslant M_2 \leqslant M_1$
III.f	III	Flat	10 $M_\odot \leqslant M_1 \leqslant 100$ $M_\odot$	10 $M_\odot \leqslant M_2 \leqslant M_1$
I.h	I	Salpeter	10 $M_\odot \leqslant M_1 \leqslant 100$ $M_\odot$	10 $M_\odot \leqslant M_2 \leqslant M_1$
I.l	I	Salpeter	1 $M_\odot \leqslant M_1 \leqslant 100$ $M_\odot$	0.5 $M_\odot \leqslant M_2 \leqslant M_1$

Table 2. The number of the compact binaries formed in each model. Each column represents the model name, and the number of NS-NSs, NS-BHs, and BH-BHs, respectively. The numbers in the parenthesis are for the case of the conservative core-merger criterion while those without the parenthesis are for the case of the optimistic core-merger criterion. The definition of optimistic and conservative core-merger criteria are shown in Sec. 2.2.3.

	NS-NS	NS-BH	BH-BH
Model III.s	5(1994)	93085 (93793)	132534 (133485)
Model III.f	0 (279)	185335 (187638)	517067 (522581)
Model I.h	58724 (60715)	73193 (76277)	108184 (108734)
Model I.l	1847 (1865)	2264 (2354)	3559 (3578)

the Pop I cases (see Figs. 6 and 7). Since the coalesce time due to the emission of the gravitational wave is proportional to $(M_1 M_2 M_{\rm total})^{-1}$ (Eq. 79), even BH-BHs with larger separations can merge within 15 Gyr for the Pop III cases. Secondly, large fraction of Pop III binaries which evolve into BH-BHs avoid the CE phase, where the separation is decreased and even core-merger occurs before the compact binary formation. While Pop I binaries with small orbital separations merge before the compact binary formation, Pop III binaries do not suffer from such merging even with small orbital separations. Thus, the number of the coalescing Pop III BH-BHs is much larger than that of Pop I case.

(2) Different initial mass range

Finally, we briefly mention the results of Model I.l, which are basically the same as Model I.h. Comparing the 3rd and 4th rows of Table 2, we find that the number of compact binaries formed in Model I.l is ~ 3 % of that in Model I.h for each compact binary. This is consistent with the ratio of the number of massive stars which form compact objects in 10 $M_\odot \leqslant M_1 \leqslant 100$ $M_\odot$ to that of 1 $M_\odot \leqslant M_1 \leqslant 100$ $M_\odot$ (~ 4 %). Moreover, the ratio of the number of coalescing compact binaries to the total number of compact binaries is the same in both models for each compact binary: ~ 30 % for NS-NSs, ~ 4 % for NS-BHs, and ~ 4 % for BH-BHs (Tables 2 and 3). It should also be noted that despite the small number of massive stars, the number of coalescing NS-NSs in Model I.l is larger than or comparable to that in Model III.s.

In these calculations, we do not take into account the angular momentum transfer due to the magnetic braking even for Models I.h and I.l. This is because we would like to clarify the qualitative difference between the two populations, by comparing the formation channels of Pop III and Pop I compact binaries under the same conditions.

4 POP III COMPACT BINARY MERGER RATE

4.1 Star formation rate of Pop III stars

In order to calculate the merger rates and history of compact binaries formed in the early universe, the information about Pop III star formation rates (SFRs) is needed. We here adopt the SFR calculated by a semi-analytical approach (de Souza, Yoshida & Ioka 2011), in which the following three effects are taken into account: (1) effect of the radiative feedback on Pop III star formation, (2) inhomogeneous reionization of the intergalactic medium (IGM), and (3) chemical evolution of the IGM.

Pop III stars (=the stars without heavy metal) are categorized into two types; Pop III.1 and Pop III.2 stars. Pop III.1 stars are the *very* first stars (Tegmark et al. 1997; Bromm, Coppi & Larson 2002; Abel, Bryan & Norman 2002; Yoshida et al. 2006). On the other hand, the Pop III.2 stars are the second generation of stars born from pristine gas affected by the some feedbacks from earlier stars, e.g., ultraviolet radiations and supernovae (SNe) (Johnson & Bromm 2006; Yoshida, Omukai & Hernquist

Table 3. The number of the compact binaries with coalescence time less than 15 Gyr among those in Table 2. Notations are the same as Table 2.

	NS-NS	NS-BH	BH-BH
Model III.s	5 (1994)	64 (164)	25536 (26468)
Model III.f	0 (279)	50 (149)	115056 (120532)
Model I.h	20149 (21155)	2703 (3664)	3928 (3976)
Model I.l	776 (785)	99 (134)	150 (151)

Table 4. The formation channels of each compact binaries which merge within 15 Gyr for the case of Model III.s. Each column represents the formation channel, the fraction which each channel occupies, and the evolution history. Here, RLOF, CE, DCE, SN, CE+SN, and DCE+SN represents the Roche lobe over flow, CE phase, double CE phase, supernova explosion or direct collapse, supernova explosion or direct collapse as soon as after the CE phase, and supernova explosion or the direct collapse as soon as after the double CE phase, respectively.

Channel	Fraction	Evolution History
NSNS 1	80.0% (0.4%)	SN:1, CE+SN:2
NSNS 2	20% (99.6%)	RLOF:1→2, SN:1, CE:2+SN:2
NSNS others	0% (0%)	The others
NSBH 1	86.8% (90.5%)	RLOF:1→2, SN:1, CE+SN:2
NSBH 2	8.8% (3.6%)	RLOF:1→2, SN:1, RLOF:2→1, SN:2
NSBH 3	2.9% (1.2%)	SN:1, CE+SN:2
NSBH 4	1.5% (0.6%)	CE:1, SN:1, RLOF:2→1, SN:2
NSBH 5	0% (1.8%)	CE:1, RLOF:1→2, SN:1, RLOF:2→1, SN:2
NSBH 6	0% (1.8%)	CE+SN:1, RLOF:2→1, SN:2
NSBH others	0% (0.5%)	The others
BHBH 1	55.3% (53.5%)	RLOF:1→2, SN:1, RLOF:2→1, SN:2
BHBH 2	13.3% (12.7%)	RLOF:1→2, SN:1, RLOF:2→1, CE+SN:2
BHBH 3	8.1% (7.9%)	RLOF:1→2, CE+SN:1, RLOF:2→1, SN:2
BHBH 4	6.2% (6.0%)	CE:1, SN:1, RLOF:2→1, SN:2
BHBH 5	5.5% (5.3%)	RLOF:1→2, CE+SN:1, RLOF:2→1, CE+SN:2
BHBH 6	2.9% (2.8%)	CE:1, SN:1, RLOF:2→1, CE+SN:2
BHBH 7	1.5% (1.7%)	CE+SN:1, RLOF:2→1, SN:2
BHBH 8	1.3% (1.3%)	RLOF:1→2, DCE+SN:1, SN:2
BHBH 9	1.1% (1.1%)	DCE+SN:1, SN:2
BHBH 10	1.1% (1.1%)	DCE, SN:1, SN:2
BHBH 11	1.1% (1.1%)	RLOF:1→2, SN:1, CE:2+SN:2
BHBH others	2.6% (5.5%)	The others

2007). We take into account the contributions from both types of Pop III stars in the Pop III SFR.

The metal enrichment in the IGM is also important. In the early universe, the metal pollution is mainly driven by the Pop III SNe (e.g., Madau, Ferrara & Rees 2001). Since the mechanisms of metal pollution are highly uncertain. de Souza, Yoshida & Ioka (2011) assumes that the metal enrichment proceeds until the region where the galactic outflows have reached. In the polluted gas, low mass Pop II stars are expected to be formed because of the efficient metal and dust cooling (Omukai et al. 2005; Schneider et al. 2006; Dopcke, Glover, Clark & Klessen 2013). In their model, the Pop III star formation turns off in metal-enriched regions by the galactic winds. The star formation rate density (comoving) is shown in figure 8. The red line is the the total SFR density of Pop III stars, and the green and blue lines are those of Pop III.1 and Pop III.2 stars, respectively.

4.2 Pop III compact binary merger rates

In this subsection, we show the history of the merger rate density of Pop III compact binaries in the universe. The merger rate density is calculated using the results in the previous section and the Pop III SFR density described in Sec. 4.1. We define $R_{\rm i}(t)$ [Myr^{-1} Mpc^{-3}] as the merger rate density at a certain age of the universe t and calculate it from

$$R_{\rm i}(t) = \int_0^t f_{\rm b} \frac{{\rm SFR}(t')}{\langle M \rangle} \frac{N_{\rm i}(t-t')}{N_{\rm total}} dt', \tag{90}$$

where the subscript i denotes the type of compact binaries (NS-NS, NS-BH, or BH-BH), $f_{\rm b}$ is the initial binary fraction here taken 1/3, $\langle M \rangle$ [M$_\odot$] is the mean initial stellar mass, SFR(t') [M$_\odot$ yr^{-1} Mpc^{-3}] is the Pop III SFR density at t', $N_{\rm total}$ is the total number of simulated stars, and $N_{\rm i}(t-t')dt'$ is the number of compact binaries which are formed during the time interval of $[t', t'+dt']$ and merge at the

Table 5. The same as Table 4, but for Model III.f.

Channel	Fraction	Evolutionary History
NSNS 2	0% (100%)	RLOF:1→2, SN:1, CE:2+SN:2
NSNS others	0% (0%)	The others
NSBH 1	54.4% (52.2%)	RLOF:1→2, SN:1, CE+SN:2
NSBH 2	12.3% (4.5%)	RLOF:1→2, SN:1, RLOF:2→1, SN:2
NSBH 3	1.7% (0.6%)	SN:1, CE+SN:2
NSBH 4	28.1% (10.2%)	CE:1, SN:1, RLOF:2→1, SN:2
NSBH 5	3.5% (29.9%)	CE:1, RLOF:1→2, SN:1, RLOF:2→1, SN:2
NSBH 6	0% (1.9%)	CE+SN:1, RLOF:2→1, SN:2
NSBH others	0% (0.7%)	The others
BHBH 1	36.9% (35.4%)	RLOF:1→2, SN:1, RLOF:2→1, SN:2
BHBH 2	16.3% (15.7%)	RLOF:1→2, SN:1, RLOF:2→1, CE+SN:2
BHBH 3	8.6% (8.3%)	RLOF:1→2, CE+SN:1, RLOF:2→1, SN:2
BHBH 4	8.5% (8.2%)	CE:1, SN:1, RLOF:2→1, SN:2
BHBH 5	11.8% (11.3%)	RLOF:1→2, CE+SN:1, RLOF:2→1, CE+SN:2
BHBH 6	6.3% (6.1%)	CE:1, SN:1, RLOF:2→1, CE+SN:2
BHBH 7	0.8% (0.9%)	CE+SN:1, RLOF:2→1, SN:2
BHBH 8	2.2% (2.1%)	RLOF:1→2, DCE+SN:1, SN:2
BHBH 9	1.9% (1.8%)	DCE+SN:1, SN:2
BHBH 10	2.3% (2.2%)	DCE, SN:1, SN:2
BHBH 11	0.8% (0.8%)	RLOF:1→2, SN:1, CE:2+SN:2
BHBH others	3.6% (7.2%)	The others

Table 6. The same as Table 4, but for Model I.h.

Channel	Fraction	Evolutionary History
NSNS 3	51.2% (49.7%)	RLOF:1→2, SN:1, CE:2, CE:2+SN:2
NSNS 4	24.7% (24.0%)	CE:1, SN:1, CE:2, CE+SN:2
NSNS 5	6.9% (8.7%)	CE:1, CE+SN:1, CE+SN:2
NSNS 6	4.5% (4.4%)	CE:1, SN:1, CE:2, RLOF:2→1 CE+SN:2
NSNS 7	4.0% (4.1%)	DCE, CE+SN:1, CE+SN:2
NSNS others	8.7% (9.1%)	The others
NSBH 7	47.7% (37.7%)	CE:1, SN:1, CE:2, CE+SN:2
NSBH 8	13.2% (13.9%)	RLOF:1→2, SN:1, CE:2, SN:2
NSBH 9	10.0%(16.2%)	CE:1, SN:1, CE:2, SN:2
NSBH 10	9.1% (10.8%)	RLOF:1→2, SN:1, CE:2, CE:2+SN:2
NSBH 11	7.5% (5.3%)	CE:1, SN:1, RLOF:2→1, CE+SN:2
NSBH others	12.5% (16.1%)	The others
BHBH 8	6.2% (6.0%)	RLOF:1→2, DCE+SN:1, SN:2
BHBH 12	80.5% (78.4%)	RLOF:1→2, SN:1, CE:2, SN:2
BHBH 13	8.4% (9.1%)	DCE+SN:1, RLOF:2→1, SN:2
BHBH others	4.9% (6.5%)	The others

time t. The resulting $R_i(t)$ is shown in Fig. 9 for the four cases with different IMFs (Salpeter or flat) and core-merger criteria (optimistic or conservative; see Sec. 2.2.3). Note that the difference in the core-merger criteria does not affect the merger rate density so much, and the difference in the IMFs varies $R_i(t)$ by a factor of five.

In Model III.s (the Salpeter IMF), the current merger rate density ($z = 0$) of Pop III BH-BHs is estimated as (see Fig. 9)

$$R_{\rm BHBH} \sim 0.012 \left(\frac{\rm SFR_p}{10^{-2.5}\ \rm M_\odot yr^{-1} Mpc^{-3}} \right) \rm Err_{sys}\ Myr^{-1} Mpc^{-3}, \quad (91)$$

where $\rm SFR_p$ is the peak value of Pop III SFR density in Fig. 8, and $\rm Err_{sys}$ is the possible systematic errors on the assumption in the Pop III binary population synthesis. $\rm Err_{sys} = 1$ corresponds to adopting distribution functions of semi-major axis a, eccentricity e, and the binary parameters for Pop I stars. Note that these might be different for Pop III stars, so that in general

Table 7. The same as Table 4, but for Model I.l.

Channel	Fraction	Evolutionary History
NSNS 3	66.9% (66.4%)	RLOF:1→2, SN:1, CE:2, CE:2+SN:2
NSNS 4	19.9% (19.7%)	CE:1, SN:1, CE:2, CE+SN:2
NSNS 5	1.1% (1.4%)	CE:1, CE+SN:1, CE+SN:2
NSNS 6	3.8% (3.7%)	CE:1, SN:1, CE:2, RLOF:2→1 CE+SN:2
NSNS 7	1.5% (1.5%)	DCE, CE+SN:1, CE+SN:2
NSNS others	7.8% (7.3%)	The others
NSBH 7	51.3% (43.5%)	CE:1, SN:1, CE:2, CE+SN:2
NSBH 8	10.1% (12.4%)	RLOF:1→2, SN:1, CE:2, SN:2
NSBH 9	10.9%(18.0%)	CE:1, SN:1, CE:2, SN:2
NSBH 10	6.7% (6.2%)	RLOF:1→2, SN:1, CE:2, CE:2+SN:2
NSBH 11	6.7% (7.5%)	CE:1, SN:1, RLOF:2→1, CE+SN:2
NSBH others	14.3% (12.4%)	The others
BHBH 12	80.0% (76.7%)	RLOF:1→2, SN:1, CE:2, SN:2
BHBH 14	11.5% (12.2%)	RLOF:1→2, SN:1, CE:2, CE:2+SN:2
BHBH others	18.5% (11.1%)	The others

$\mathrm{Err_{sys}} \neq 1$. Adopting that the number density of galaxies is $n_{\rm galaxy} \sim 0.01$ Mpc^{-3} (Cross et al. 2001), the galactic merger rate of Pop III BH-BHs is estimated as $R_{\rm BHBH,gal} \sim 1.2$ Myr^{-1} galaxy^{-1}. For Model III.f (the flat IMF), the current merger rate density of the Pop III BH-BHs is estimated as $R_{\rm BHBH} \sim 0.025$ Myr^{-1}Mpc^{-3}, and the galactic merger rate as $R_{\rm BHBH,gal} \sim 2.5$ Myr^{-1} galaxy^{-1}. It is worth to note that these rates are an order of magnitude smaller than the lower limits of the merger rate of the NS-NSs derived from the observed NS-NSs (Kalogera, Kim, Lorimer et al. 2004b). We also note that although the number of merging BH-BHs is ~ 4 times larger for Model III.s than for Model III.s from Table 3, the merger rate is only a factor 2 larger. This comes from the difference in the mass distribution (see Figs. 6 and 7).

4.3 Expected cumulative distribution as a function of cosmological z

First of all, from the chirp signal of a coalescing compact binary, we obtain the redshifted mass $M_{1z} = (1+z)M_1$, $M_{2z} = (1+z)M_2$ and the amplitude of the gravitational waves which is proportional to $M_{cz}^{5/6}/d_{\rm L}(z)$, where M_{cz} is the redshifted chirp mass defined by $(M_{1z}^{3/5}M_{2z}^{3/5})(M_{1z}+M_{2z})^{-1/5}$ and the luminosity distance ($d_{\rm L}(z)$) (Seto, Kawamura & Nakamura 2001). The luminosity distance is defined by

$$d_{\rm L}(z) = \frac{c}{H_0}(1+z)\int_0^z \frac{dz}{\sqrt{\Omega_{\rm m}(1+z)^3+\Omega_\Lambda}}, \tag{92}$$

where $c, H_0, \Omega_{\rm m}$ and Ω_Λ are the light velocity, the present Hubble parameter, the matter density parameter and the dark energy parameter, respectively. These values are now well determined (Planck Collaboration 2013) so that we have the three relations among three unknown variables, M_1, M_2 and z, respectively. Then we can determine the values of M_1, M_2 and z, even if we can not determine the redshift of the host galaxy or even if we can not determine the angular position of the observed compact binary precisely by identifying the host galaxy. The error of these values are order $(\mathrm{S/N})^{-1}$. The comoving distance for a given redshift z is defined by

$$r(z) = \frac{c}{H_0}\int_0^z \frac{dz}{\sqrt{\Omega_{\rm m}(1+z)^3+\Omega_\Lambda}}. \tag{93}$$

Now writing the merger rate of a Pop III BH-BH per comoving volume as $R_m(z)$, we have the observed cumulative redshift number distribution of the coalescing Pop III BH-BHs $N(z)$ as

$$N(z) = 4\pi\int_0^z R_m(z) r(z)^2 \frac{1}{1+z}\frac{dr}{dz}dz, \tag{94}$$

where $1/(1+z)$ is the effect of the cosmological time dilation. From Fig. 9 (a) and (b), we can regard that $R_m(z)$ is essentially constant up to $z \sim 1$, so that we expect roughly

$$N(z) \propto \int_0^z r(z)^2 \frac{1}{1+z}\frac{dr}{dz}dz. \tag{95}$$

The above equation shows that the cumulative distribution of Pop III coalescing BH-BHs depends roughly only on the cosmological parameters $\Omega_{\rm m}, \Omega_\Lambda$ and z. Figure 10 shows the z dependence of Eq. (95). From our simulations, the typical mass of Pop III black hole is ~ 30 M$_\odot$ which is much larger than the Pop I black hole of mass ~ 10 M$_\odot$ so that we can identify the Pop III black hole by the determination of the mass. From Fig. 9, the merger rate of Pop III BH-BHs per comoving volume up to $z \sim 1$ is essentially constant. The expected event rate of the coalescing Pop III BH-BHs by KAGRA, Adv. LIGO, Adv. Virgo and GEO network is ~ 140 (68) yr^{-1} up to ~ 1500 Mpc ($z = 0.28$) for the flat (Salpeter) IMF with the fiducial parameter values of $\mathrm{SFR_p} \sim 10^{-2.5}$ M$_\odot$yr^{-1}Mpc^{-3} and $\mathrm{Err_{sys}} = 1$. Therefore, by checking if the observed cumulative redshift distribution agrees with the results of our simulations, we can confirm the existence of Pop III massive stars. By the third generation of the detectors such as Einstein Telescope (ET)[8], we expect

[8] http://www.et-gw.eu

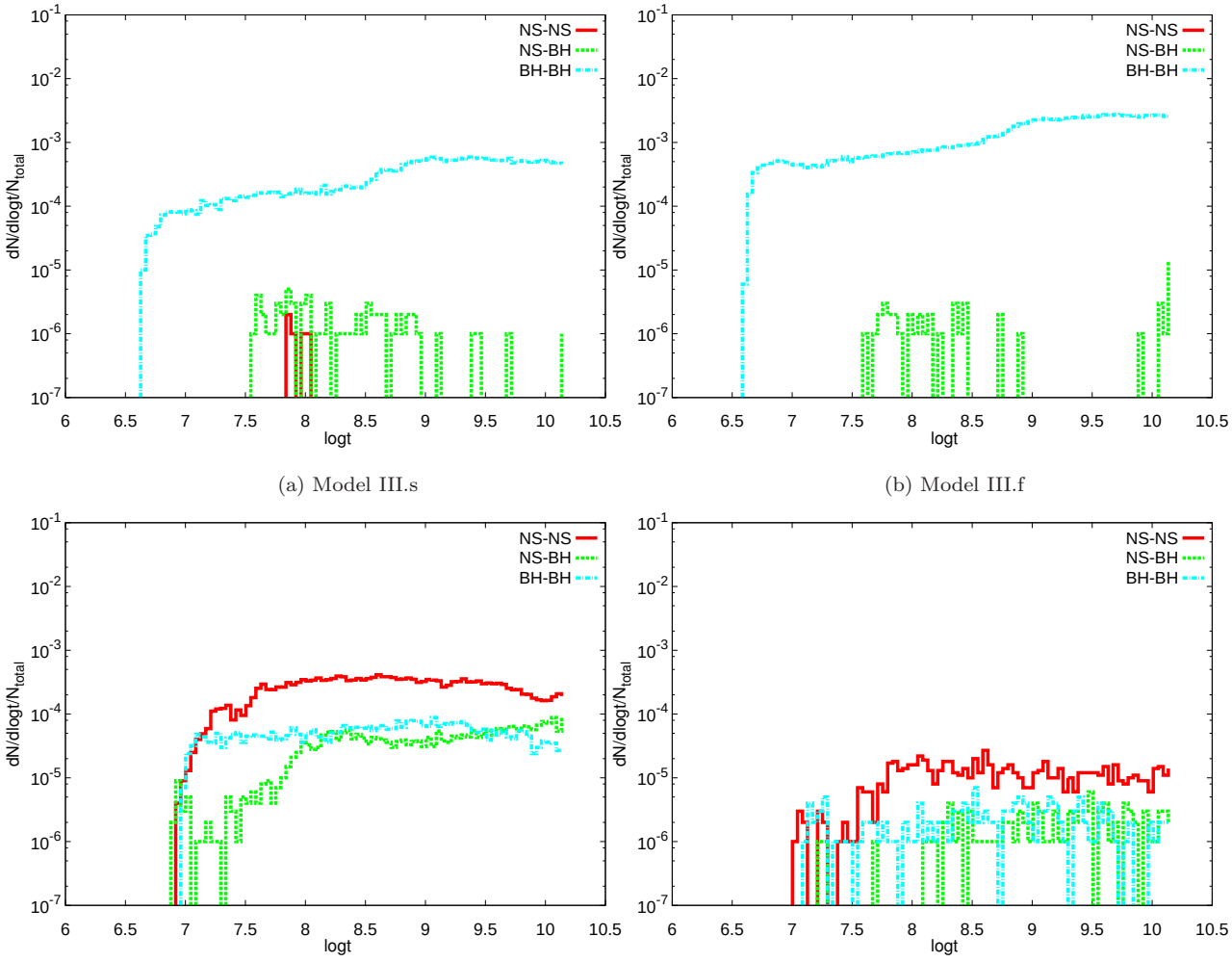

(a) Model III.s

(b) Model III.f

(c) Model I.h

(d) Model I.l

Figure 5. The normalized coalescence time distribution of compact binaries for each model. Each panel corresponds to Models III.s (a), III.f (b), I.h (c), and I.l (d), respectively. In each figure, the red, green, and blue lines correspond to the NS-NSs, NS-BHs, and BH-BHs, respectively.

~ 80 times more events per year up to $z \sim 3$ so that we might see the evolution of the merger rate and determine the Pop III IMF from the difference of detection rate. Note that the expected rate of 2.5 $(1.2) \times 10^{-8}$ events yr^{-1} Mpc^{-3} for the flat (Salpeter) IMF with the fiducial parameter values is consistent with the upper limit of $\sim 10^{-7}$ events yr^{-1} Mpc^{-3} by LIGO-Virgo(S6/VSR2/VSR3) (Aasi et al. 2013). In reality, however, we should consider the mass of each black hole, the inclination angle of the binary orbit, position of the detector and the detector noise spectrum so that we need to perform Monte Carlo simulations to obtain the expected cumulative redshift distribution (Kanda et al. in preparation).

5 DISCUSSION

In this paper, we do not include the magnetic braking since Pop III stars are formed from the primordial no metal gas. However, there are discussions against this assumption. Among them, the enhancement of the magnetic field during the star formation has been well studied using the numerical simulations (e.g., Maki & Susa 2004; Machida et al. 2008; Machida & Doi 2013). According to their results, the turbulent motions driven in the galaxy formation might increase the magnetic field up to $< 10^{-6}$ G (Schleicher et al. 2010; Sur et al. 2010; Schober et al. 2012; Turk et al. 2012), which is similar value to that in molecular clouds of the galaxy. If this is the case, we should include the effect of magnetic braking, which will give rise $\mathrm{Err}_{\mathrm{sys}} \neq 1$.

Dominik et al. (2012) discussed the metallicity dependence of the compact binary merger by focusing on Pop I stars with metallicities $Z_\odot$ and 0.1 $Z_\odot$. Here, we compare our results for the coalescing Pop III BH-BHs with those in Dominik et al. (2012) and discuss the implications of our results (see Table 8). In Table 8, the second and third columns show the results of Dominik et al. (2012) for

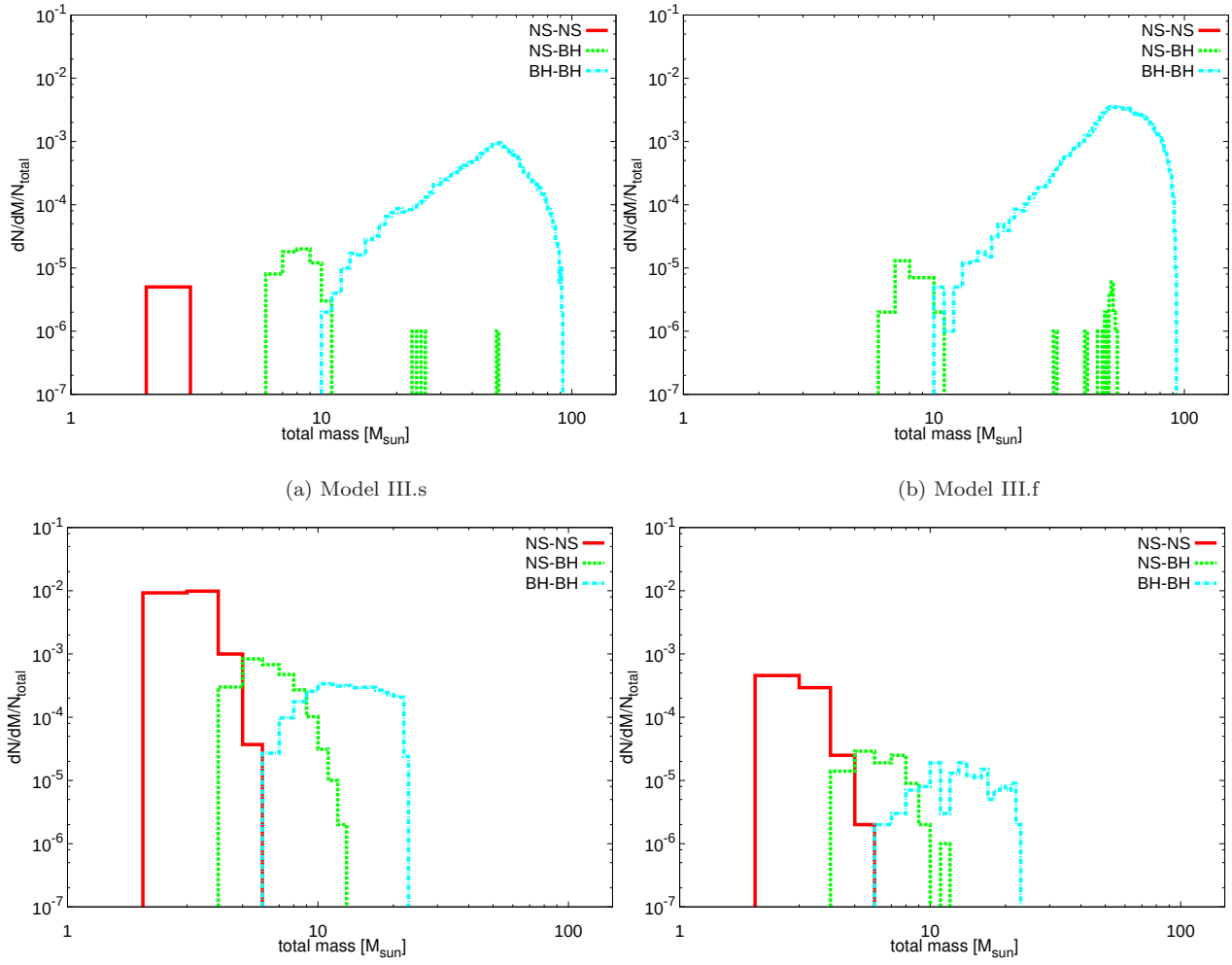

(a) Model III.s

(b) Model III.f

(c) Model I.h

(d) Model I.l

Figure 6. The normalized distribution of the total mass ($M_{\rm tot} = M_1 + M_2$) of compact binaries for each model . Each panel corresponds to Models III.s (a), III.f (b), I.h (c), and I.l (d), respectively. In each figure, the red, green, and blue lines correspond to the NS-NSs, NS-BHs, and BH-BHs, respectively.

metallicity $Z_\odot$ and 0.1 $Z_\odot$ stars. Here, Models A and B correspond to the standard case of submodels A and B in Dominik et al. (2012). The last column show our results for Pop III binaries, where we take the fiducial parameter values: $\mathrm{Err_{sys}} = 1$ and $\mathrm{SFR_p} = 10^{-2.5}$ $\mathrm{M_\odot\ yr^{-1}\ Mpc^{-3}}$. As in Table 8, Dominik et al. (2012) suggested that for Pop I stars with $Z = Z_\odot$, the merger rate of the BH-BHs becomes 8.2 (1.9)$\times 10^{-8}$ events $\mathrm{yr^{-1}\ Mpc^{-3}}$ in their Model A (Model B), respectively, while for Pop I stars with $Z = 0.1\ Z_\odot$, it becomes 7.33 (1.36) $\times\ 10^{-7}$ events $\mathrm{yr^{-1}\ Mpc^{-3}}$ in their Model A (Model B), respectively. Here we assume that the galaxy with metallicity $Z = 0.1\ Z_\odot$ has the hypothetical number density $\sim 10^{-2}$ $\mathrm{Mpc^{-3}}$ in order to compare the results. On the other hand, for our Pop III BH-BHs, the expected merger rate is 2.5 (1.2) $\times\ 10^{-8}$ events $\mathrm{yr^{-1}\ Mpc^{-3}}$ for the flat (Salpeter) IMF, respectively. This means that the merger rate of the Pop III BH-BHs is smaller than that of Pop I. However, for Pop I BH-BHs with metallicity $Z = Z_\odot$ (0.1 $Z_\odot$), the typical chirp mass is 6.7 (13.2) $M_\odot$, while for Pop III ones it is ~ 30 $M_\odot$ as we showed in Fig. 7. Since the detection range of merger events increases in proportion to $M_{\rm chirp}^{5/6}$, the detection rate increases in proportion to $M_{\rm chirp}^{5/2}$. Therefore, the detectable event rate of the Pop III BH-BHs is 13 (6) times larger for the flat (Salpeter) IMF than that of Pop I with $Z = Z_\odot$ in Model A, while it is 0.26 (0.13) times larger than that of Pop I with $Z = 0.1\ Z_\odot$, if the galaxy consists of stars with $Z = 0.1\ Z_\odot$. In Model B, these numbers become 56 (26) for $Z = Z_\odot$ case and 1.4 (0.7) for $Z = 0.1\ Z_\odot$ case, respectively. Thus, for the fiducial parameters of Pop III binaries, the contribution of Pop III BH-BHs is comparable to or larger than that of Pop I with $Z = Z_\odot$ and 0.1 $Z_\odot$, since the major part of a galaxy does not necessarily consist of Pop I stars with $Z = 0.1\ Z_\odot$.

While Dominik et al. (2012) did not take account of the evolution of the star formation rate, Dominik et al. (2013)

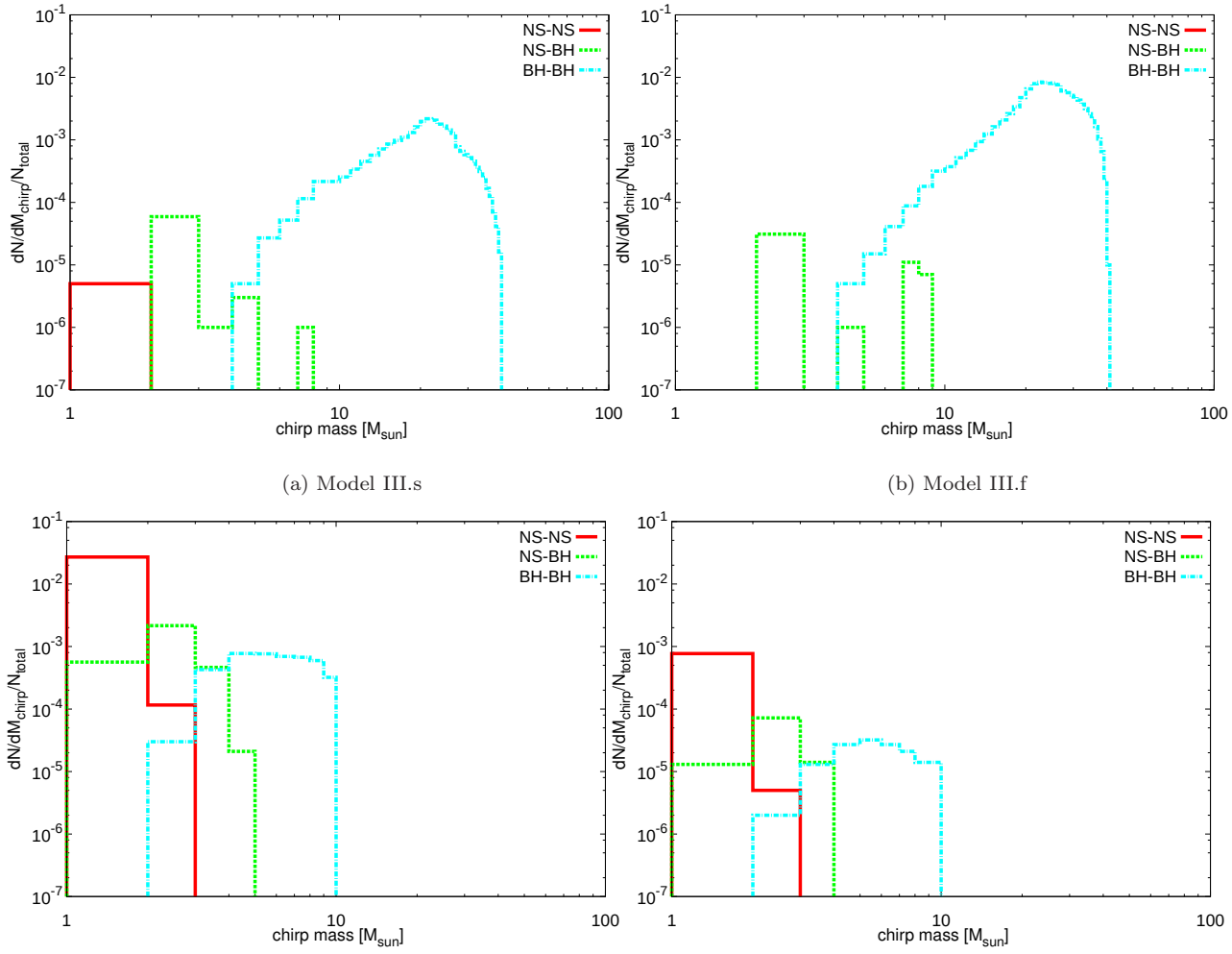

(a) Model III.s

(b) Model III.f

(c) Model I.h

(d) Model I.l

Figure 7. The same as Fig. 6, but for distribution of the chirp mass ($M_{\rm chirp} = (M_1 M_2)^{3/5}/(M_1 + M_2)^{1/5}$).

Table 8. The comparison of the merger rate density of the BH-BHs and typical chirp mass between previous studies and our study. The second and third columns show the results of Dominik et al. (2012) for metallicity $Z_\odot$ and 0.1 $Z_\odot$ stars. Here, Models A and B correspond to the standard case of submodels A and B in Dominik et al. (2012). The last column show our results for Pop III binaries. Here, we take the fiducial parameter values: $\mathrm{Err_{sys}} = 1$ and $\mathrm{SFR_p} = 10^{-2.5}$ $\mathrm{M_\odot\ yr^{-1}\ Mpc^{-3}}$.

	$Z_\odot$	0.1 $Z_\odot$	Pop III
Model A [10^{-8} events $\mathrm{yr^{-1}\ Mpc^{-3}}$]	8.2	73.3	2.5 (flat)
Model B [10^{-8} events $\mathrm{yr^{-1}\ Mpc^{-3}}$]	1.9	13.6	1.2 (Salpeter)
chirp mass [$\mathrm{M_\odot}$]	6.7	13.2	30

adopted a certain model of the star formation rate (Eq. 1 of Dominik et al. 2013) and the metallicity Z evolution (Eqs. 3 to 5 of Dominik et al. 2013) to compute the cumulative redshift distribution of the coalescing compact binaries. They also took into account the lower metal stars such as Pop II and even those with $Z < 10^{-4}$ $Z_\odot$, but not completely metal-free stars, Pop III.1 and Pop III.2 stars. The star formation rate expressed by Eq. (1) in Dominik et al. (2013) is completely different from the one shown in Fig. 8 of the present paper. In the latter case, the star formation rate at $z = 0$ is zero, while in the former case, it is the present star formation rate of our Galaxy which is not zero.

In Fig. 6 of Dominik et al. (2013), they show the cumulative merger rate as a function of redshift z for different four models which corresponds to Fig. 10 of the present paper. In our Fig. 10, for the second (third) generation gravita-

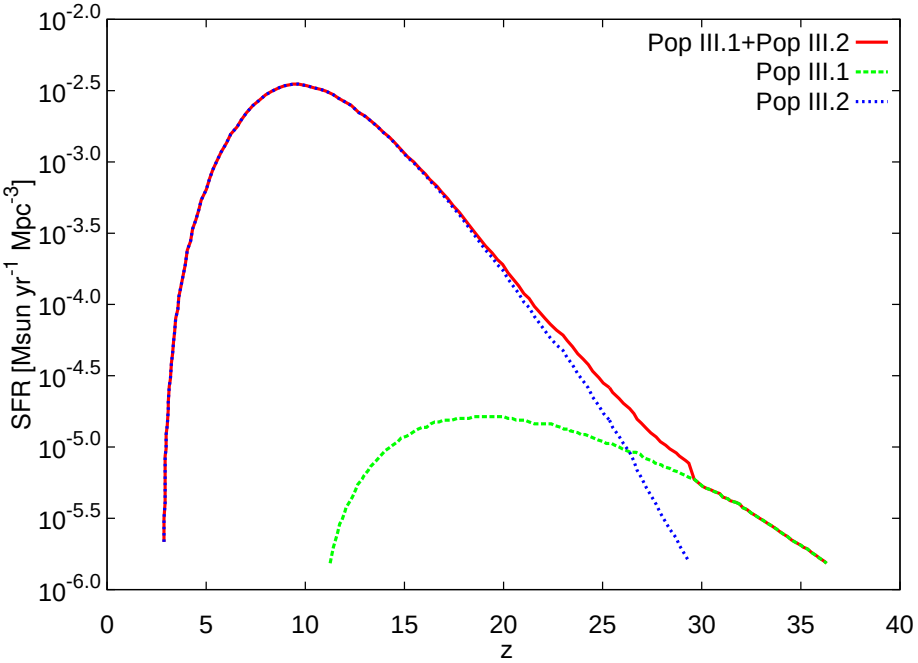

Figure 8. The star formation rate density (comoving) calculated by de Souza et al. (2011). The unit of the rate is $M_\odot$ per comoving volume per proper time. The red line is the the total SFR density of Pop III stars, and the green and blue lines are those of Pop III.1 and Pop III.2 stars, respectively.

tional wave detectors, $z \sim 0.3$ (3) is the detection range, respectively. In Fig. 6 of Dominik et al. (2013), information on the detectability is not available, since the chirp mass distribution function is not available. Assuming it is similar to that in Dominik et al. (2012), the merger rate for the second and third generation gravitational wave detectors is either higher or lower than Fig. 10 of the present paper taking into account that the chirp mass of Pop I and Pop II BH-BHs is smaller than that for Pop III.1 and Pop III.2 BH-BHs. If the detection rate of the coalescing Pop I and Pop II BH-BHs is lower than that of Pop III, it might be possible to confirm the existence of the massive Pop III stars by detecting gravitational waves from their remnant black hole and identifying the typical chirp mass ~ 30 $M_\odot$ and the cumulative redshift distribution which depends almost only on the cosmological parameters. On the other hand, if the detection rate of the coalescing Pop I and Pop II BH-BHs is higher, Pop III BH-BHs contribute only some parts of the gravitational wave events of BH-BHs. If the detected number is $\sim 10^4$ for the third generation detector like ET, we might select a Pop III BH-BH from its mass and be able to draw the cumulative redshift distribution function to confirm the existence of Pop III stars. In any case, it is needless to say that there are many undetermined parameters and distribution functions for the Pop III population synthesis so that more theoretical study on the evolution and initial conditions of Pop III binaries including the star formation rate is urgent.

ACKNOWLEDGEMENTS

We thank Jarrod R. Hurley, Christopher A. Tout and Krzysztof Belczynski, Nobuyuki Kanda and Kei Tanaka for useful comments and Sanemichi Takahashi and Sho Fujibayashi for help of debugging of numerical codes. This work is supported in part by the Grant-in-Aid from the Ministry of Education, Culture, Sports, Science and Technology (MEXT) of Japan, No.25-1284 (T.K.), No.23-838 (K.I.), No.24-1772 (K.H.), No.23540305 (T.N.) and No.24103006 (T.N.).

APPENDIX

A.1 The stellar radius and age after the mass transfer

In this section, we describe how to calculate the stellar radius and other stellar properties after the mass transfer. After the mass transfer, the primary mass and the secondary mass change and these changes affect the stellar evolutions. In some case, the mass losing star becomes the naked-He star losing its H-envelope. The evolution of a naked-He star is well represented by that of a He star (Kippenhahn & Weigert 1990). However, for a Pop III star, the numerical calculation of a He main sequence evolution is not presented in the literature. So, in this paper, we follow the evolution of a naked-He star using the fitting formulae of Hurley, Pols & Tout (2000) with $Z = 10^{-4}$.

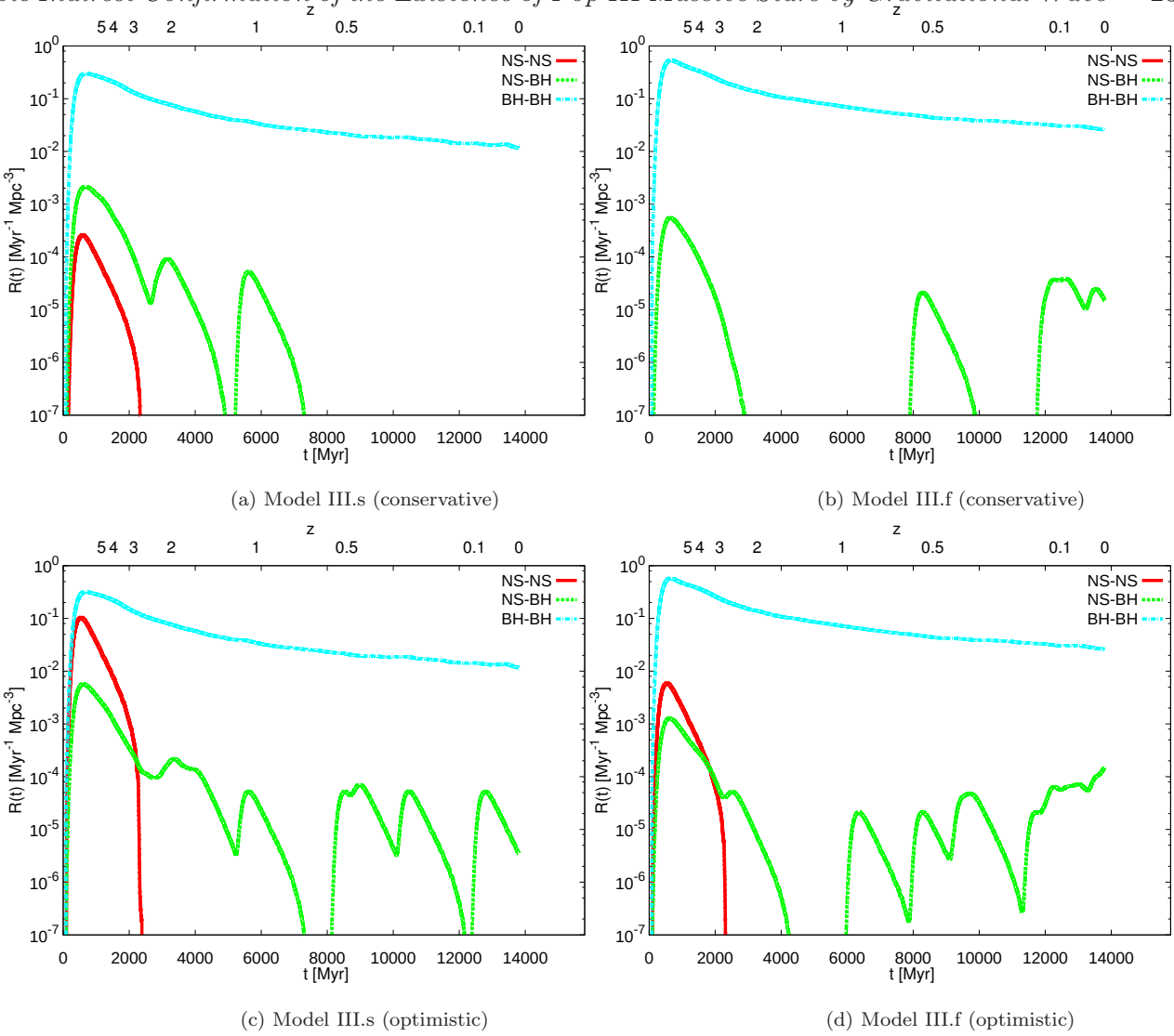

(a) Model III.s (conservative)

(b) Model III.f (conservative)

(c) Model III.s (optimistic)

(d) Model III.f (optimistic)

Figure 9. The evolution of merger rate density of each compact binary. In this figure, the left panels are Model III.s (Salpeter IMF) with conservative (a) and optimistic (c) core-merger criteria described in Sec. 2.2.3. The right panels, (b) and (d) are the same as left ones but for Model III.f (flat IMF). In each panel, the red, green, and blue lines correspond to the NS-NSs, NS-BHs, and BH-BHs, respectively.

(1)Main sequence

We consider main sequence like stars, that is, the main sequence and naked He main sequence. For example, if the main sequence star which has the convective core gains mass due to the mass transfer from the companion giant star, it will get mass and mix the H in the convective core so that the star will appear younger. Thus, the radius after the mass transfer of δM is calculated as $R_{\rm fit}(M+\delta M, t'(M, M+\delta M, t))$ where $t'(M, M+\delta M, t)$ is the correction of the stellar age due to the mass gain. In order to treat this rejuvenation, we use the approximation by Hurley et al. (2002). Hurley's approximation treat the rejuvenation as three cases below (For details, see Hurley et al. 2002, Hurley et al. 2000, Tout et al. 1997).

Firstly, we consider that the main sequence star which has the convective core gains or loses the mass. Assuming that the convective core mass and the fraction of the burnt hydrogen fuel at the core are proportional to the stellar mass and the fraction of the main sequence lifetime $\tau_{\rm H} = t/t_{\rm H}$, respectively, we have that the burnt H-mass at the convective core is proportional to $M\tau_{\rm H}$. Since the burnt H-mass at the convective core does not change before and after the mass transfer, we have

$$M\frac{t}{t_{\rm H}(M)} = (M+\delta M)\frac{t'}{t_{\rm H}(M+\delta M)}. \tag{96}$$

Therefore, the effective age t' is

$$t' = \frac{M}{M+\delta M}\frac{t_{\rm H}(M+\delta M)}{t_{\rm H}(M)}t, \tag{97}$$

and the stellar radius after the mass transfer is calculated as $R_{\rm fit}(M+\delta M, t'(M, M+\delta M, t))$.

Secondly, we consider that the naked He main sequence star gets the mass from the naked He giant star. In the same

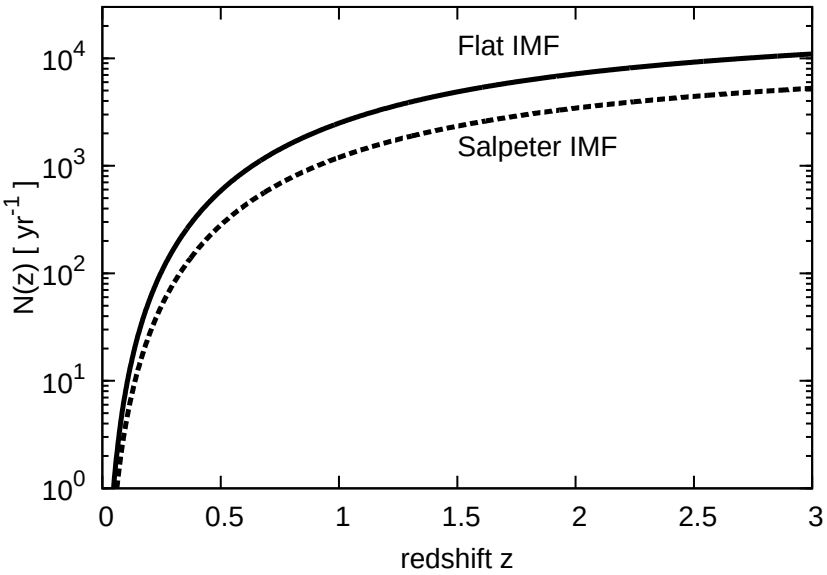

Figure 10. The expected cumulative redshift distribution of the merger rate of the Pop III BH-BHs $N(z)$. The solid and dashed lines correspond to the flat and Salpeter IMF, respectively. Here, we assume that the merger rate density $R_{\rm m}$ of 30 $M_\odot$BH $-$ 30 $M_\odot$BH remains constant with redshift. Although the constant $R_{\rm m}$ is a good approximation for $z < 1$, for $z > 1$, $R_{\rm m}$ increases as can be seen in Fig. 9 so that the event rate is larger than this figure for $z > 1$.

way as the main sequence, we approximate

$$t' = \frac{M}{M+\delta M}\frac{t_{\rm HeMS}(M+\delta M)}{t_{\rm HeMS}(M)}t, \tag{98}$$

where

$$\left(\frac{t_{\rm HeMS}}{\rm Myr}\right) = \frac{0.4129 + 18.81(M/{\rm M}_\odot)^4 + 1.853(M/{\rm M}_\odot)^6}{(M/{\rm M}_\odot)^{6.5}}, \tag{99}$$

is the naked He main sequence star lifetime (Hurley et al. 2000). The stellar radius after the mass transfer is calculated as $R_{\rm fit}(M+\delta M, t'(M, M+\delta M, t))$.

Thirdly, if the naked He main sequence star gets the H-rich envelope due to the mass transfer, the star becomes the He-burning star. Under the same assumption as the case of the main sequence, the core mass of the new He-burning star is the same as the naked He main sequence star mass. Then the age of the He-burning star is approximated as

$$t' = t_{\rm H}(M+\delta M) + \frac{t_{\rm He}(M+\delta M)}{t_{\rm HeMS}(M)}t. \tag{100}$$

In this case, the stellar radius after the mass transfer is calculated by the same method as the giant star below.

(2) The giant stars

For a giant star, we assume that the stellar age is decided by the core mass which is not affected by the mass transfer at the envelope. Therefore, we do not change the age of the giant star at the mass transfer. However the stellar radius changes due to the change of the mass ratio of the core to the envelope. In order to calculate the radius of the giant which is in the thermal equilibrium state after the star loses the envelope due to the mass transfer, we use the Hurley's formula (Hurley et al. 2000).

If the star loses the envelope mass, we calculate

$$\mu = \left(\frac{M-M_{\rm c}}{M}\right)\min\left[5.0, \max\left(1.2, \left(\frac{L}{L_0}\right)^{-1/2}\right)\right], \tag{101}$$

where $L_0 = 7.0\times10^4$ $L_\odot$ for giant stars which have the H-envelope and

$$\mu = 5\left(\frac{M-M_{\rm c}}{M}\right), \tag{102}$$

for naked He giant stars. Then if $\mu < 1.0$ we calculate the radius as

$$R_{\rm th} = R_{\rm c}(M_{\rm c})\left(\frac{R_{\rm fit}(M+\delta M, t+\delta t)}{R_{\rm c}(M_{\rm c})}\right)^r, \tag{103}$$

where $R_{\rm fit}(M,t)$ is calculated using fitting formulae (Section 2.1.2),

$$r = \frac{\left(1+c^3\right)(\mu/c)^3\,\mu^{\rm fac}}{1+(\mu/c)^3}, \tag{104}$$

with

$$c = 0.006, \tag{105}$$

$$\rm fac = \min\left[0.1/\ln\left(\frac{R}{R_{\rm c}}\right), \frac{-14}{\log\mu}\right]. \tag{106}$$

In our calculation, the ratio of the stellar envelope mass to the total mass is typically about 1/2, i.e., $\mu \simeq 1/2$ and $\rm fac = 0.1/(\ln(R/R_c) \simeq 0.1/(\ln(100)) \simeq 0.02$. Thus, the exponent of perturbation is typically $r \simeq \mu^{\rm fac} \simeq 1$. Therefore, $R_{\rm th} \simeq R_{\rm fit}(M+\delta M, t+\delta t)$.

Table 9. The models

code	model A	model B	model C	model D	model E	model F
Tidal evolution	ON	OFF	ON	ON	ON	ON
α	3.0	3.0	1.0	3.0	3.0	3.0
e	0	0	0	0	0	Eq.85
M_2	Eq.84	Eq.84	Eq.84	Eq.82	Eq.84	Eq.84
Z	0.02	0.02	0.02	0.02	0.0001	0.02

Table 10. The comparison with Hurley's code

code	model A	model B	model C	model D	model E	model F
Hurley et al. (2002)	1.131×10^{-1}	1.229×10^{-1}	7.572×10^{-2}	1.334×10^{-2}	2.290×10^{-1}	8.631×10^{-2}
Hurley's open code	1.683×10^{-1}	1.799×10^{-1}	1.197×10^{-1}	4.389×10^{-2}	2.851×10^{-1}	1.399×10^{-1}
Our code	1.189×10^{-1}	1.270×10^{-1}	8.491×10^{-2}	1.031×10^{-2}	2.293×10^{-1}	9.065×10^{-2}

A.2 The comparison with Hurley's code

Hurley's binary evolution open code has a number of differences from BSE code in Hurley et al. (2002) (Private communication with Hurley and Tout). The main differences of codes are the following. First, in Hurley's binary evolution open code, CE parameter λ is not constant. Hurley fitted λ as a function of mass and luminosity and rewrote the code. Second, they changed the treatments of compact remnant mass from the formula of Hurley et al. (2002) to Belczynski et al. (2002). Furthermore, there are a lot of differences smaller than above two differences. So we show the difference in the number of compact binary between Hurley et al. (2002), Hurley's binary evolution open code and our binary evolution model (see Section2.2). We use the number of Pop I white dwarf-white dwarf (WD-WD) binaries in order to compare the binary evolution codes. We use six models. In these models, there are differences in five quantities such as the tidal evolution effect, the CE parameter α, the initial eccentricity, the initial secondary mass and the metallicity (See Table 9, Hurley, Tout & Pols (2002)). We show the comparison of WD-WD formation rates in Table 10. We can see that results of Hurley, Tout & Pols (2002) agree rather well with ours.

A.3 The convergence check

In order to check whether the results depend on the total number of the binaries, we calculate how many compact binaries can merge within 15 Gyr for Model III.s setting $N_{\rm total} = 10^5$, 10^6, and 10^7. The result is shown in Table 11

We assume that the result for $N_{\rm total} = 10^7$ is the correct one and check the convergence of the results for $N_{\rm total} = 10^6$ and 10^5 using the Poisson distribution. First, we consider the result of NS-NSs. In the case of 10^6 binaries, the expected mean of the number of the coalescing NS-NSs is $n_{\rm NSNS} = 27/10 = 2.7$. The number of the NS-NSs for $N_{\rm total} = 10^6$ is 5, which is within 2σ error, i.e., $n_{\rm NSNS} \pm 2\sqrt{n_{\rm NSNS}}$=2.7±3.2. Next, for NS-BHs and BH-BHs, the expected mean of the numbers are $n_{\rm NSBH} = 56.2$ and $n_{\rm BHBH} = 25434.6$, respectively. Our results (64 and 25536) are within 1σ error, i.e., $n_{\rm NSBH} \pm \sqrt{n_{\rm NSBH}}$=$56.2 \pm 7.5$ and $n_{\rm BHBH} \pm \sqrt{n_{\rm BHBH}}$=$25434.6 \pm 159.5$ Similar argument can be done for the results of 10^5 binaries. In conclusion the convergence of the results is confirmed within 1σ statistical error except for small number of events like NS-NSs.

REFERENCES

Aasi, J. et al. 2013, PRD, 87, 022002

Abel, T., Bryan, G. L., & Norman, M. L. 2002, Science, 295, 93

Abt, H. A. 1983, ARA&A, 21, 343

Accadia, T., Acernese, F., Antonucci, F., et al. 2011, Classical and Quantum Gravity, 28, 114002

Amaro-Seoane, P., Aoudia, S., Babak, S., et al. 2013, GW Notes, Vol. 6, p. 4-110, 6, 4

Baraffe, I., Heger, A., & Woosley, S. E. 2001, ApJ, 550, 890

Belczynski, K., Kalogera, V., & Bulik, T. 2002, ApJ, 572, 407

Belczynski, K., Bulik, T., & Rudak, B. 2004, ApJL, 608, L45

Belczynski, K., Taam, R. E., Kalogera, V., Rasio, F. A., & Bulik, T. 2007, ApJ, 662, 504

Belczynski, K., Kalogera, V., Rasio, F. A., et al. 2008, ApJS, 174, 223

Belczynski, K., & Dominik, M. 2012, arXiv:1208.0358

Bromm, V., Coppi, P. S.,& Larson, R. B. 2002, ApJ, 564, 23

Bulik, T., Belczyński, K., & Rudak, B. 2004, A&A, 415, 407

Cameron, A. G. W. 1967, Nature, 215, 464

Cappellaro, E., Turatto, M., Tsvetkov, D. Y., et al. 1997, A & A, 322, 431

Cappellaro, E., Evans, R., & Turatto, M. 1999, A & A, 351, 459

Table 11. The convergence check of Monte Carlo simulations for Model III.s. Each column means the number of binaries, the number of the coalescing NS-NSs, NS-BHs, and BH-BHs, respectively.

Total number	NSNS	NSBH	BHBH
10^5	0	11	2593
10^6	5	64	25536
10^7	27	562	254346

Clark, P. C., Glover, S. C. O., Klessen, R. S., & Bromm, V. 2011, ApJ, 727, 110

Coward, D.M. , Howell, E.J., Piran, T. et al. 2012, MNRAS, 425, 2668

Cross, N., Driver, S. P., Couch, W., et al. 2001, MNRAS, 324, 825

de Souza, R. S., Yoshida, N., & Ioka, K. 2011, A&A, 533, A32

Doi, K., & Susa, H. 2011, ApJ, 741, 93

Dominik, M., Belczynski, K., Fryer, C., et al. 2012, ApJ, 759, 52

Dominik, M., Belczynski, K., Fryer, C., et al. 2013, ApJ, 779, 72

Dopcke, G., Glover, S. C. O., Clark, P. C., & Klessen, R. S. 2013, ApJ, 766, 103

Duquennoy, A., Mayor, M., & Halbwachs, J.-L. 1991, A&AS, 88, 281

Eggleton P.P.,1983, ApJ, 268, 368

Fryer, C. L. 1999, ApJ, 522, 413

Fryer, C. L., Belczynski, K., Wiktorowicz, G., et al. 2012, ApJ, 749, 91

Greif, T. H., Bromm, V.,Clark, P. C., et al. 2012, MNRAS, 424, 399

Grindlay, J., Portegies Zwart, S. & McMillan, S. 2006, Nature Phys., 2, 116

Heggie, D. C. 1975, MNRAS, 173, 729

Hjellming, M. S., & Webbink, R. F. 1987, ApJ, 318, 794

Hjellming, M. S. 1989, Ph.D. Thesis,

Hirano, S., Hosokawa, T., Yoshida, N., et al. 2013, arXiv:1308.4456

Hosokawa, T., Omukai, K., Yoshida, N., & Yorke, H. W. 2011, Science, 334, 1250

Hosokawa, T., Yoshida, N., Omukai, K., & Yorke, H. W. 2012, ApJL, 760, L37

Hurley, J. R., Pols, O. R., & Tout, C. A. 2000, MNRAS, 315, 543

Hurley, J. R., Tout, C. A., & Pols, O. R. 2002, MNRAS, 329, 897

Hut, P. 1981, A&A, 99, 126

Inayoshi, K., Hosokawa, T., & Omukai, K. 2013, MNRAS, 431, 3036

Ivanova, N., Podsiadlowski, P., & Spruit, H. 2002, MNRAS, 334, 819

Ivanova, N., Heinke, C. O., Rasio, F. A. et al. 2008, MNRAS, 386, 553

Johnson, J. L., & Bromm, V. 2006, MNRAS, 366, 247

Kalogera, V., Kim, C., Lorimer, D. R. et al. 2004, ApJ, 601, L179

Kalogera, V., Kim, C., Lorimer, D. R. et al. 2004, ApJ, 614, L137

Kawamura, S., Ando, M., Seto, N., et al. 2011, Classical and Quantum Gravity, 28, 094011

Kippenhahn, R., & Weigert, A. 1990, Stellar Structure and Evolution, Springer-Verlag Berlin Heidelberg New York. Also Astronomy and Astrophysics Library,

Kobulnicky, H. A., & Fryer, C. L. 2007, ApJ, 670, 747

Kobulnicky, H. A., Smullen, R. A., Kiminki, D. C., et al. 2012, ApJ, 756, 50

Kowalska, I., Bulik, T., & Belczynski, K. 2012, A&A, 541, A120

Kulsrud, R. M., Cen, R., Ostriker, J. P., & Ryu, D. 1997, ApJ, 480, 481

Langer, M., Puget, J.-L., & Aghanim, N. 2003, PRD, 67, 043505

Li, W., Chornock, R., Leaman, J., et al. 2011, MNRAS, 412, 1473

Loveridge, A. J., van der Sluys, M. V., & Kalogera, V. 2011, ApJ, 743, 49

Machida, M. N., Omukai, K., Matsumoto, T., & Inutsuka, S.-i. 2008, ApJ, 677, 813

Machida, M. N., Matsumoto, T., & Inutsuka, S.-i. 2008, ApJ, 685, 690

Machida, M. N., & Doi, K. 2013, MNRAS, 435, 3283

Madau, P., Ferrara, A., & Rees, M. J. 2001, ApJ, 555, 92

Maki, H., & Susa, H. 2004, ApJ, 609, 467

Marigo, P., Girardi, L., Chiosi, C., & Wood, P. R. 2001, A&A, 371, 152

Matsumoto, M. & Nishimura, T., 1998, TOMACS, 8, 1, 3

McKee, C. F., & Tan,J. C. 2008, ApJ, 681, 771

Omukai, K., & Nishi,R. 1998, ApJ, 508, 141

Omukai, K., Tsuribe, T., Schneider, R., & Ferrara, A. 2005, ApJ, 626, 627

Paczyński, B., & Sienkiewicz, R. 1972, Acta Astronomica, 22, 73

Paczynski, B. 1976, Structure and Evolution of Close Binary Systems, 73, 75

Peters, P. C., & Mathews, J. 1963, Physical Review, 131, 435

Peters, P. C. 1964, Physical Review, 136, 1224

Planck Collaboration, Ade, P. A. R., Aghanim, N., et al. 2013, arXiv:1303.5076

Podsiadlowski, P., Ivanova, N., Justham, S., & Rappaport, S. 2010, MNRAS, 406, 840

Prince, T. A., Anderson, S. B., Kulkarni, S. R.& Wolszczan, A. 1991, ApJ, 374, L41

Pudritz, R. E., & Silk, J. 1989, ApJ, 342, 650

Punturo, M., Abernathy, M., Acernese, F., et al. 2010, Classical and Quantum Gravity, 27, 194002
Rasio, F. A., Tout, C. A., Lubow, S. H., & Livio, M. 1996, ApJ, 470, 1187
Salpeter, E. E. 1955, ApJ, 121, 161
Schaerer, D. 2002, A&A, 382, 28
Schleicher, D. R. G., Banerjee, R., Sur, S., et al. 2010, A & A, 522, A115
Schneider, R., Omukai, K., Inoue, A. K., & Ferrara, A. 2006, MNRAS, 369, 1437
Schober, J., Schleicher, D., Federrath, C., et al. 2012, ApJ, 754, 99
Seto, N., Kawamura, S., & Nakamura, T. 2001, Physical Review Letters, 87, 221103
Stacy, A., Greif, T. H., & Bromm, V. 2010, MNRAS, 403, 45
Stacy, A., Greif, T. H., & Bromm, V. 2012, MNRAS, 422, 290
Stothers, R. 1966, ApJ, 144, 959
Sur, S., Schleicher, D. R. G., Banerjee, R., Federrath, C., & Klessen, R. S. 2010, ApJL, 721, L134
Tegmark, M., Silk, J., Rees, M. J., et al. 1997, ApJ, 474, 1
Timmes, F. X., Woosley, S. E., & Weaver, T. A. 1996, ApJ, 457, 834
Tout, C. A., Aarseth, S. J., Pols, O. R., & Eggleton, P. P. 1997, MNRAS, 291, 732
Turk, M. J., Oishi, J. S., Abel, T., & Bryan, G. L. 2012, ApJ, 745, 154
Verbunt, F., & Phinney, E. S. 1995, A&A, 296, 709
Webbink, R. F. 1984, ApJ, 277, 355
Webbink, R. F. 1985, Interacting Binary Stars, 39
Webbink, R. F. 1988, IAU Colloq. 103: The Symbiotic Phenomenon, 311
Widrow, L. M. 2002, Reviews of Modern Physics, 74, 775
Woosley, S. E. 1986, Saas-Fee Advanced Course 16: Nucleosynthesis and Chemical Evolution, 1
Xu, X.-J., & Li, X.-D. 2010, ApJ, 716, 114
Yoshida, N., Omukai, K., Hernquist, L., & Abel, T. 2006, ApJ, 652, 6
Yoshida, N., Omukai, K., & Hernquist, L. 2007, ApJL, 667, L117
Yoshida, N., Omukai,K., & Hernquist, L. 2008, Science, 321, 669
Zahn, J.-P. 1975, A&A, 41, 329
Zahn, J.-P. 1977, A&A, 57, 383